JASA ARTICLE

Passive acoustic characterization of sub-seasonal sound speed variations in a coastal ocean[a)]

Tsu Wei Tan[1,b)] and Oleg A. Godin[2,c)]
[1]*Department of Marine Science, ROC Naval Academy, 813 Kaohsiung, Taiwan*
[2]*Department of Physics, Naval Postgraduate School, 833 Dyer Road, Monterey, California 93943-5216, USA*

ABSTRACT:
Acoustic noise interferometry is applied to retrieve empirical Green's functions (EGFs) from the ambient and shipping noise data acquired in the Shallow Water 2006 experiment on the continental shelf off New Jersey. Despite strong internal wave-induced perturbations of the sound speed in water, EGFs are found on 31 acoustic paths by cross-correlating the noise recorded on a single hydrophone with noise on the hydrophones of a horizontal linear array about 3.6 km away. Datasets from two non-overlapping 15-day observation periods are considered. Dispersion curves of three low-order normal modes at frequencies below 110 Hz are extracted from the EGFs with the time-warping technique. The dispersion curves from the first dataset were previously employed to estimate the seabed properties. Here, using this seabed model, we invert the differences between the dispersion curves obtained from the two datasets for the variation of the time-averaged sound speed profile (SSP) in water between the two observation periods. Results of the passive SSP inversion of the second dataset are compared with the ground truth derived from *in situ* temperature measurements. The effect of temporal variability of the water column during noise-averaging time on EGF retrieval is discussed and quantified. © *2021 Acoustical Society of America*.
https://doi.org/10.1121/10.0006664
(Received 23 June 2021; revised 16 September 2021; accepted 21 September 2021; published online 13 October 2021)
[Editor: Stan E. Dosso] Pages: 2717–2737

I. INTRODUCTION

Ocean acoustic noise interferometry (NI) retrieves an estimate of deterministic Green's function from time series of diffuse shipping and ambient noise recorded at spatially separated, synchronized hydrophones (Roux *et al.*, 2004; Sabra *et al.*, 2005b; 2005a; Godin, 2006) or vector sensors (Zhou *et al.*, 2017; Nichols *et al.*, 2019). The Green's function estimate that is obtained from noise cross-correlations is referred to as the empirical Green's function (EGF) (Fried *et al.*, 2008; Brooks and Gerstoft, 2009; Godin, 2009; Brown *et al.*, 2014). EGFs approximate the Green's function even when the noise is not perfectly diffuse (Godin, 2009; Weaver *et al.*, 2009; Godin, 2010; Godin *et al.*, 2010; Skarsoulis and Cornuelle, 2019, 2020) and the environment evolves during the noise averaging time (Godin, 2018). Thus, NI offers an environmentally friendly and cost-effective way of acoustic remote sensing of the ocean that avoids the use of any controlled sound sources and minimizes the disruption of biologically important natural soundscapes.

In addition to the environmental information along the sound propagation paths connecting the receivers, noise cross correlation functions (NCCFs) and EGFs contain information about the geometry of the receiving system, which can be used for array element localization (Sabra *et al.*, 2005c; Nowakowski *et al.*, 2015), and information about the time shift and drift of clocks on spatially separated receivers, which can be used for the clocks' synchronization (Sabra *et al.*, 2005c; Godin *et al.*, 2014).

Obtaining passive measurements of acoustic quantities, such as acoustic travel times, with the high accuracy required for oceanographic applications, is challenging. Only some of the EGFs measured with NI have been successfully used to meaningfully characterize the underwater propagation environment. Passive ocean acoustic tomography was first demonstrated in deep water using direct ray arrivals between receivers on vertical line arrays (VLAs) (Godin *et al.*, 2010). Evers *et al.* (2017) resolved the group speed dispersion between sound in 3–5 and 5–10 Hz frequency bands over 126 km, deep-water propagation path. Woolfe *et al.* (2015) were the first to demonstrate passive acoustic thermometry of the ocean and measured with high sensitivity the spatially averaged deep-water temperature variations along two propagation paths in the Atlantic and Pacific oceans. In shallow water, passive acoustic measurements of the spatially averaged sound speed were reported, and passive acoustic thermometry was demonstrated by Li *et al.* (2019) and Li *et al.* (2021). By assimilating satellite and *in situ* temperature measurements, they also restored the sound speed profile (SSP) (Li *et al.*, 2019). Passive acoustic measurements of the depth-averaged velocity of ocean currents were carried out in the Straits of Florida (Godin *et al.*, 2014). Goncharov *et al.* (2016) applied the ray tomography

[a)]Parts of this work have been previously reported at the 179th Meeting of the Acoustical Society of America (Virtual, December 2020).
[b)]Electronic mail: ttan1@nps.edu, ORCID: 0000-0002-1145-9349.
[c)]ORCID: 0000-0003-4599-2149.

approach to the same measured EGFs to retrieve the sound speed and current velocity profiles, with the results proving more reliable for current velocity than for sound speed. Compressional wave velocity in the bottom near the seafloor was evaluated from the head-wave component of the EGF (Yang *et al.*, 2020). Parabolic-equation and normal-mode-based geoacoustic inversions of the passively measured EGFs were reported for sites in the Straits of Florida (Zang *et al.*, 2015; Brown *et al.*, 2016; Godin *et al.*, 2017; Tan *et al.*, 2019) and in the Mid-Atlantic Bight (Qin *et al.*, 2017; Tan *et al.*, 2020). Passive acoustic characterization of the seabed at other locations was obtained with the passive fathometer technique (Siderius *et al.*, 2006; Gerstoft *et al.*, 2008; Harrison and Siderius, 2008; Siderius *et al.*, 2010; Yardim *et al.*, 2014), which is related to NI.

Tan *et al.* (2020) applied NI to measure EGFs and retrieve geoacoustic parameters of the seabed on the continental shelf off New Jersey. The time series of underwater noise were used, which had been nearly continuously recorded in the Shallow Water 2006 (SW06) experiment during a fifteen-day observation period. Time warping (Bonnel *et al.*, 2020b) was applied to the EGFs to passively measure normal mode dispersion curves, which served as the input data for the geoacoustic inversion (Tan *et al.*, 2020). In this paper, we build on this recent research and extend it to characterize temporal variations in the water column properties using NI. We compare the EGFs, which are retrieved from two non-overlapping fifteen-day observation periods, invert the difference in the modal dispersion curves for the SSP in the water column, and compare the results of the passive acoustic measurements with the ground truth provided by *in situ* temperature sensors. The passive acoustic characterization of the sub-seasonal water column variations is made particularly challenging by transient, short-term sound speed variations due to the strong internal wave and internal tide activity at the site of the SW06 experiment.

The remainder of this work is presented as follows. In Sec. II, the SW06 experiment is briefly introduced, *in situ* sound-speed measurements are described, and calculation and features of the NCCFs are discussed. Section III describes retrieval of normal mode dispersion curves from measured NCCFs and includes an analysis of the effects of the short-term temporal variability and range dependence of the SW06 environment on mode travel times. Consistency of the environmental information contained in the NCCFs, which are obtained in different observation periods, is illustrated in the Appendix by comparing the results of the geoacoustic inversions with input data provided by different NCCFs. The inverse problem of extracting the unknown SSP in water from passively measured modal dispersion curves is formulated and solved in Sec. IV. The ground truth, which is provided by *in situ* measurements, is employed in Sec. V to evaluate results of the passive SSP inversion. Section VI summarizes conclusions of this work.

II. EXPERIMENTAL DATA AND NCCFS

A. SW06

The data of this work come from the recording of ambient and shipping noise in the SW06 experiment (Newhall *et al.*, 2007; Tang *et al.*, 2007) on the continental shelf off the New Jersey Coast, about 220 km from New York Harbor [Fig 1(a)]. The time series of noise were nearly continuously recorded during a 30-d period, from August 3 to September 1, 2006, on a Single Hydrophone Receiving Unit (SHRU) and a 32-hydrophone horizontal line array (HLA) of length 465 m as shown in Fig. 1(b). The hydrophones of the HLA were spaced 15 m apart, and the horizontal ranges from the SHRU to the HLA hydrophones were between 3.4 (SHRU

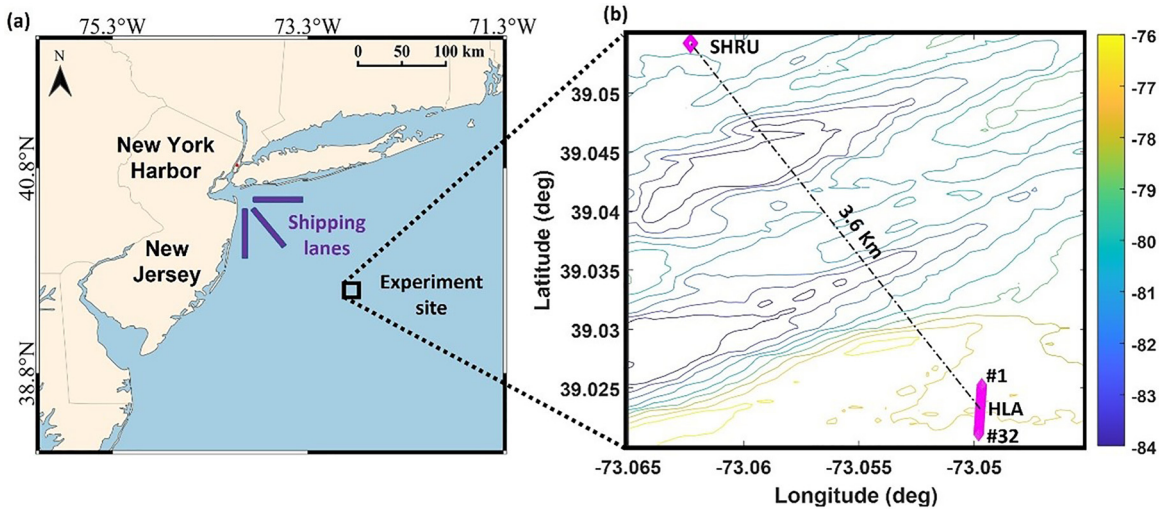

FIG. 1. (Color online) Experimental site and the locations of the receivers. (a) The site where noise records were acquired in the course of the SW06 experiment. The shipping lanes are shown leading to and from New York Harbor. (b) The SHRU and the HLA of 32 hydrophones separated about 3.6 km were employed in this work. Water depth in meters is shown by color-coded isobaths.

https://doi.org/10.1121/10.0006664

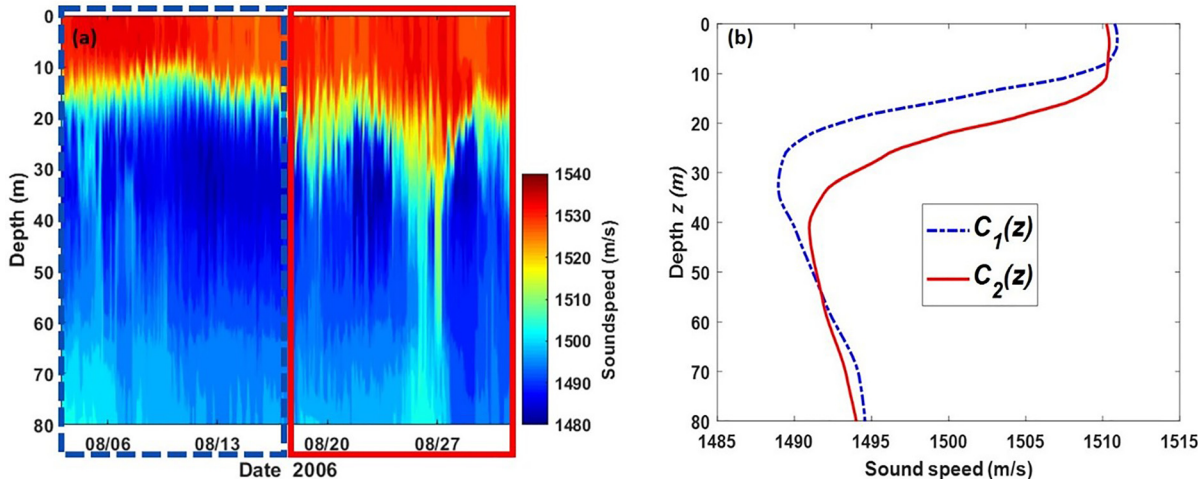

FIG. 2. (Color online) SSPs measured *in situ*. (a) Time-dependence of SSPs in water measured in August 2006 using a thermistor chain located near the HLA. The first and the second 15-day observation periods are indicated by the dashed and solid boxes, and sound speeds inside represent the SSPs of 1st and 2nd observation periods, respectively. (b) The 15-day time averages $C_1(z)$ and $C_2(z)$ of the SSPs measured during the 1st and 2nd observation periods.

to HLA #1) and 3.8 (SHRU to HLA #32) km [Fig. 1(b)]. The SHRU and HLA hydrophones were located at water depths of 78 and 77 m, respectively, close to the seafloor. Both systems had the same sampling frequency of 9765.625 Hz and readout data format (Newhall *et al.*, 2007), which helped the processing of NI.

B. Temporal variability of the environment

The SW06 site is known for strong and rapid variations of the sound speed in the water column due to energetic internal gravity waves, including internal tides (Tang *et al.*, 2007), resulting in strong transient acoustic noise bursts (Katsnelson *et al.*, 2021). One original purpose of the SW06 experiment was to study the non-linear internal waves (NLIWs) and their acoustic effects. The NLIWs in the SW06 experiment were generated by the semidiurnal barotropic tide in a water depth of about 100 m and propagated nearly parallel to the across-shelf direction, which is along the HLA-SHRU line shown in Fig. 1(b). Figure 2 shows the 30-d sound speed measured with a vertical thermistor chain (Newhall *et al.*, 2007) that was deployed in the vicinity of the southern end of the HLA. Internal tides depress the thermocline by tens of meters in a quasi-periodic manner, causing sound speed variations up to 13 m/s from the mean at a fixed depth [Fig. 2(a)] and making the environment rather challenging for the application of acoustic NI, which requires a certain time average.

This 30-d noise data, measured from the SHRU and HLA 32-hydrophone are divided into two halves for analysis: NCCF_1 and NCCF_2. The noise data of the 2nd observation period (NCCF_2) were used in the previous work to passively retrieve the geoacoustic parameters of seabed GM_2, including sediment layer thickness, compression sound speed in the sediment and basement, and density ratios (Tan *et al.*, 2020), with its average SSP measured *in situ* was taken as known and abbreviated as $C_2(z)$. Here, we take this previously inverted geoacoustic properties GM_2 and apply these to the noise data of the 1st observation period (NCCF_1), to passively invert the average SSP of the 1st observation period, abbreviated as $C_1(z)$ [Fig. 2(b)]. The seabed properties shall remain fairly unchanged within either 15-day observation period such that $\mathrm{GM}_1 \approx \mathrm{GM}_2$ and are discussed in the Appendix. For convenience, notations are organized into a list in Table I; the inverse procedure to retrieve seabed properties and SSP will be discussed later in Sec. IV.

C. Temporal variability of the NCCF

Underwater noise is a result of interference of acoustic waves that are generated by multiple natural and man-made sound sources widely spatially distributed on the ocean surface, on the seafloor, and in the water column. A signal to probe the propagation environment can be retrieved from the random ambient sound field by calculating the cross correlation function of acoustic pressure recorded concurrently at spatially separated points. We apply previously published methods (Godin *et al.*, 2014; Tan *et al.*, 2019; Tan *et al.*, 2020) to evaluate the cross correlation functions between the noise at the SHRU and each of the HLA hydrophones (Figs. 3 and 4). The NCCF between the SHRU and the *i*-th

TABLE I. List of notations.

15-day observation period	NCCF	Average sound speed profile	Inferred geoacoustic properties of seabed
1st (08/03-08/17/2006)	NCCF_1 [see Fig. 4(a)]	$C_1(z)$ [see Fig. 2(b)]	GM_1 (Appendix)
2nd (08/18-09/01/2006)	NCCF_2 [see Fig. 4(b)]	$C_2(z)$ [see Fig. 2(b)]	GM_2 (Tan *et al.*, 2020)

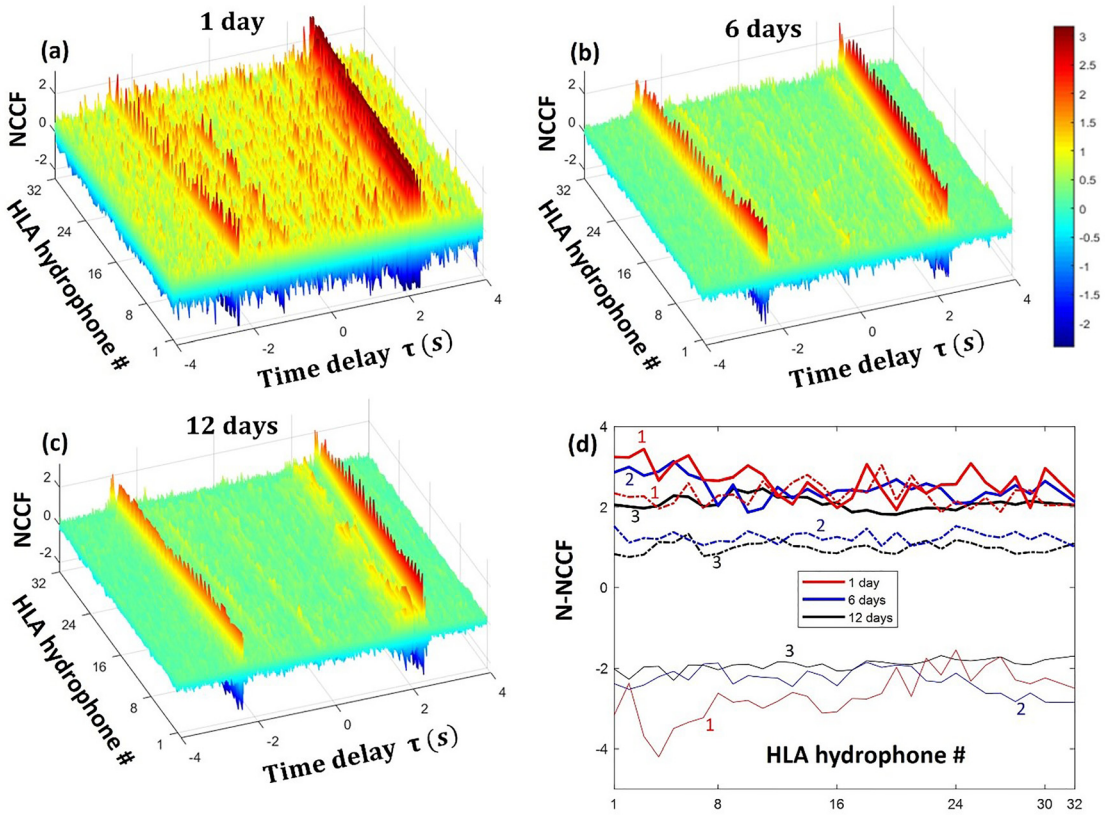

FIG. 3. (Color online) Multiple two-point NCCFs measured during the SW06 experiment. NCCFs in the same arbitrary units between the SHRU and individual hydrophones of the HLA are shown as functions of the time delay τ in seconds and the number, from 1 to 32, of the HLA hydrophone. NCCFs are calculated using different time frames for (a) 1, (b) 6, and (c) 12 days in the noise records of the 1st observation period ($NCCF_1$). (d) Maxima (thick solid lines) and minima (thin solid lines) at $-0.22\,\text{s} < \tau < -0.29\,\text{s}$, and maxima of the absolute value at $-2.00\,\text{s} < \tau < 0$ (dashed lines) of $NCCF_1$, are shown for 31 HLA hydrophones and three noise averaging times of one (1), six (2), and 12 (3) days.

hydrophone of HLA is calculated in the frequency domain as $CF_i(f)$ by averaging over N non-overlapping timeframes (64 s each) of the noise records,

$$\widehat{CF}_i(f) = \frac{1}{N}\sum_{n=1}^{N}\frac{P_S^{(n)}(f)P_{H,i}^{(n)}(f)^*}{|P_S^{(n)}(f)P_{H,i}^{(n)}(f)^*|}, \quad i = 1, 2, \ldots, 32. \tag{1}$$

Here, $P_S^{(n)}(f)$ and $P_{H,i}^{(n)}(f)$ are the spectra of noise pressure recorded during the nth time window by the SHRU and the ith HLA hydrophone, respectively, and $P_{H,i}^{(n)}(f)^*$ is the complex conjugate of $P_{H,i}^{(n)}(f)$. Note that the spectral prewhitening procedure is applied in Eq. (1) by normalizing the spectra in each timeframe by their frequency-dependent absolute values. This procedure helps to suppress the

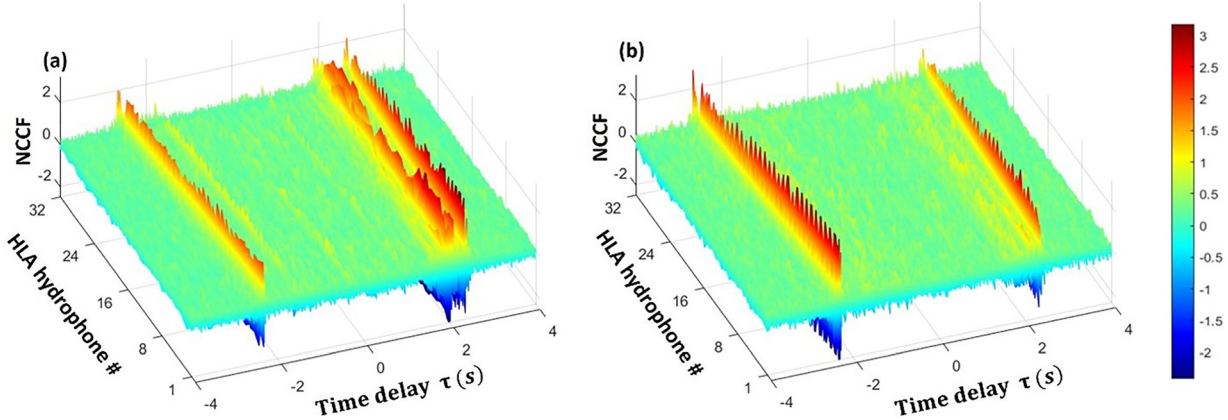

FIG. 4. (Color online) NCCFs obtained by averaging fifteen days of noise records. The process is the same as in Fig. 3 but uses all noise records during (a) the first ($NCCF_1$) and (b) the second ($NCCF_2$) observation period.

https://doi.org/10.1121/10.0006664

influence of strong, transient non-diffuse noise sources such as nearby shipping (Godin *et al.*, 2010; Godin *et al.*, 2014). The time domain NCCF, $CF_i(\tau)$, is obtained *via* the inverse Fourier transform of $\widehat{CF}_i(f)$. For brevity, the negative ($\tau < 0$) and positive ($\tau > 0$) time-delay parts of $CF_i(\tau)$ are abbreviated as N-NCCF and P-NCCF, respectively. N-NCCF and P-NCCF describe propagation from the *i*th HLA hydrophone to the SHRU and from the SHRU to the hydrophone, respectively (Roux *et al.*, 2004; Sabra *et al.*, 2005a; Godin, 2006).

The data from HLA hydrophone #31 [Fig. 1(b)] were discarded due to inconsistencies with other data (Brooks and Gerstoft, 2009) and did not produce useable information. Therefore, a total of 31 NCCFs were obtained excluding the #31 pair (Fig. 3). Theoretical NCCFs of diffuse noise are even functions of τ (Roux *et al.*, 2004; Godin, 2006) in a motionless media, but it was observed originally that all 31 measured NCCFs have a constant time shift along the τ axis. This is because a time shift exists between the clocks of the SHRU and the HLA (Tan *et al.*, 2020). The amount of time shift can be discovered by cross-correlating the P-NCCF with the N-NCCF for the same hydrophone-pair and taking the average of all pairs. The time delay axis was recalibrated with 0.896 s. This amount is much smaller than the timeframes (64 s) used in Eq. (1) and thus has a negligible impact on the quality of the NCCF.

In a time-independent ocean, Eq. (1) is expected to converge to a deterministic NCCF, when the number of timeframes is sufficiently large (Sabra *et al.*, 2005b; Godin *et al.*, 2010). Figure 3 shows the evolution of the time-domain NCCF estimate based on Eq. (1) for 31 receiver pairs, when the noise averaging time increases from 1 to 6 days, and then 12 days, starting from 3 August 2006. The frequency band $10\,\text{Hz} < f < 110\,\text{Hz}$ is used to obtain the time-domain NCCFs in Figs. 3 and 4.

The deterministic features of the NCCFs progressively arise from the random background as more daily averages are stacked (Fig. 3). The NCCFs' deterministic components most clearly manifest as the high peaks and deep troughs around the time delays $\tau = \pm 2.4$ s, which roughly correspond to each hydrophone pair's range divided by the sound speed (Fig. 3). The peaks and troughs gradually and systematically shift to larger $|\tau|$ with the increasing range (Figs. 3 and 4). The deterministic features of all NCCFs emerge from the random background after one day of noise averaging [Fig. 3(a)]. Comparison of Figs. 3(b) and 3(c) shows that a stable estimate of all 31 NCCFs is reached with noise averaging over the first 6 days (3–8 August) of the 1st observation period. Inclusion of additional 6 days of observations further suppresses the random components and increases the amplitude contrast between the deterministic and random components of the NCCFs estimates, essentially without changing the positions or shapes of the deterministic features [Fig. 3(d)]. For the same hydrophone pairs, a longer accumulation time of about 10 days (18–27 August) is needed from the start of the 2nd observation period to reach a similarly stable NCCF estimate (Tan *et al.*, 2020).

Because the noise sources are intermittent, the prominence of the stable, deterministic features of either P-NCCFs or N-NCCFs does not increase monotonically at finer time scales. In the observation period starting from 3 August 2006, P-NCCFs accumulate faster than N-NCCFs in Fig. 3(a) and then both become qualitatively stable in a similar way as more timeframes are stacked. It is also observed that on some days, shorter-term, one-day noise averages result in the N-NCCF or P-NCCF estimates that have particularly pronounced deterministic features and high contrast between the deterministic and random NCCF components. Noise averaging over a few such "good days" results in NCCF estimates that are very close to the much longer, fifteen-day averages shown in Fig. 4.

In addition to symmetric peaks at positive and negative time delays, fifteen-day noise averages (Figs. 4 and 5) reveal additional peaks at $\tau > 0$ that precede the main arrival of P-NCCF. In Figs. 5(a)–5(c), the additional peaks of P-NCCF can be clearly seen around $\tau = 2$ s, while the symmetric peaks appear around $|\tau| = 2.2$–2.7 s. The asymmetrical precursor peaks in the NCCFs are due to a persistent non-diffuse noise source in the SW06 experiment and are usually referred to as spurious arrivals (Godin *et al.*, 2010). These peaks will be discussed in Sec. II E.

D. Spatial variability and bandwidth of NCCF

Retrieving EGFs in as wide frequency band as possible is critical for passive acoustic characterization of the ocean and particularly for SSP measurements. Variation of the environmental parameters during the noise averaging period tends to destroy noise coherence at higher frequencies (Brown *et al.*, 2014; Godin, 2018). By comparing the NCCF estimates Eq. (1) that are calculated in different frequency bands, it has been found that, with noise averaging periods between 1 and 15 days, acoustic frequencies above 110 Hz do not contribute appreciably to the NCCFs' deterministic features. For the receiver pairs and the noise averaging periods considered in this study, no discernable deterministic features emerge when the pressure records are high-pass filtered at or above 110 Hz. Therefore, all calculations of NCCFs (Figs. 3–5) and their analysis in this paper is limited to the 10–110 Hz frequency band. This band extends to somewhat higher frequencies than in Brooks and Gerstoft (2009) and is the same as in Tan *et al.* (2020).

NCCFs between the SHRU and the HLA hydrophones in Figs. 3 and 4 give EGFs at 31 different ranges and 62 different azimuthal propagation directions. The variation of the amplitude of the deterministic features of NCCFs along the HLA becomes increasingly smooth as the averaging time increases. This is illustrated in Fig. 3(d), where amplitudes of the main peaks and troughs of 31 N-NCCFs are shown by solid lines; see also Fig. 5. Such behavior is expected for the diffuse noise contributions to NCCFs. The remaining, gradual variation of the NCCF amplitudes across the HLA in Fig. 3(d) can be attributed to several factors, including range dependence of the deterministic Green's function (Roux

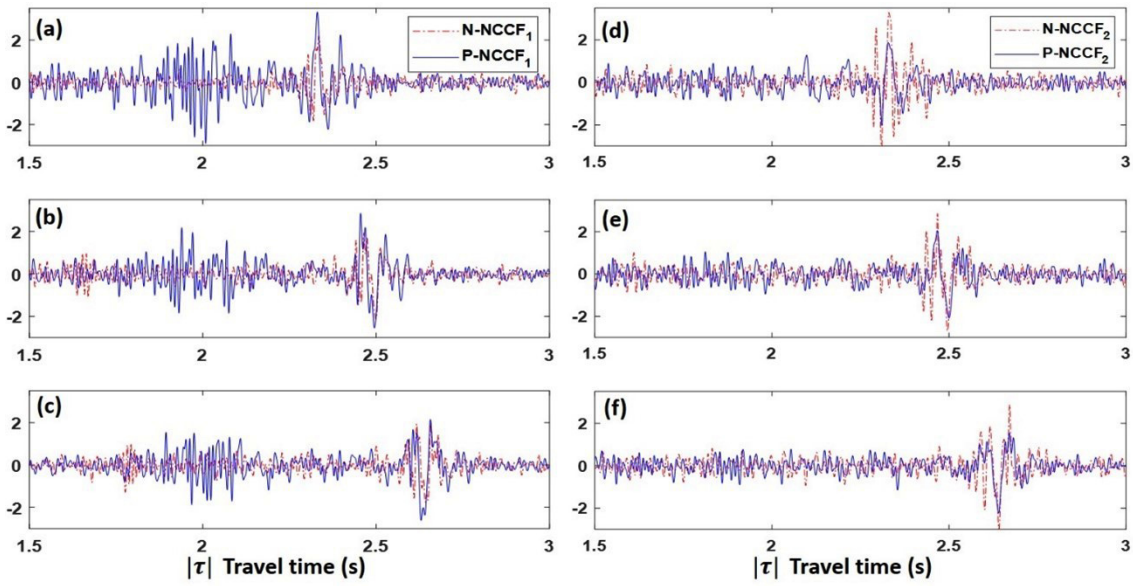

FIG. 5. (Color online) Individual waveforms of the 15-day averaged NCCFs. (a)–(c) $NCCF_1$ for the first observation period [Fig. 4(a)], obtained using HLA hydrophones 1, 16, and 32, respectively. The negative-time-delay parts ($N\text{-}NCCF_1$) and the positive-time-delay parts ($P\text{-}NCCF_1$) of $NCCF_1$ are shown by dashed and solid lines, respectively. The absolute value of time delay $|\tau|$ corresponds to the physical travel time in the empirical Green's function. (d)–(f) Same as in (a)–(c) but for $NCCF_2$, obtained in the second observation period and shown in Fig. 4(b).

et al., 2004; Godin, 2006), noise directionality in the horizontal plane (Godin, 2006; Wapenaar and Thorbecke, 2013; Godin *et al.*, 2014), and the additional EGF attenuation due to temporal variability of the ocean (Godin, 2018). The difference in amplitudes of the deterministic components of the P-NCCFs and N-NCCFs is clearly due to noise directionality in the horizontal plane. On the other hand, the differences in range and azimuthal direction from the SHRU to the northern and southern ends of the HLA [Fig. 1(b)] appear to be too small to reliably identify the mechanism responsible for the observed weak variation of the N-NCCF and P-NCCF amplitudes along the HLA.

E. Spurious arrival at NCCF

There are additional NCCFs' peaks forming up a line that appears at positive time delays τ before the main peaks of P-NCCFs in Fig. 4(a). These additional peaks are particularly visible at P-NCCF in Figs. 5(a)–5(c) and are more pronounced on the northern side of the HLA [Fig. 1(b)]. These additional peaks are identified as spurious arrival due to persistent low-frequency shipping noise from New York Harbor located about 115 NM from the experiment site. This phenomenon of spurious precursory arrival was also observed in the NCCF at different time delays τ from different hydrophone-pairs in the SW06 experiment by Qin *et al.* (2017) and Brooks and Gerstoft (2009).

The spurious arrivals partially overlap with the main peaks and distort the P-NCCFs, especially on the northern side of the HLA [Fig. 1(b)]. Because of this, the previous study and this work use only N-NCCFs as the input data to retrieve normal mode dispersion curves and perform inversions to retrieve seabed properties (Tan *et al.*, 2020) and the SSP.

In the cross correlation function of acoustic pressure recorded by two hydrophones, a non-diffuse noise component due to a compact source in the far field manifests itself as a single peak, which occurs at a time delay with magnitude less than or equal to the magnitude of the time delays of the symmetrically located peaks due to diffuse noise (Roux *et al.*, 2004; Sabra *et al.*, 2005c; Godin *et al.*, 2010). Having an additional peak of NCCF, usually referred to as spurious arrival, with the time delay magnitude less than that of the symmetric peaks, is a sign of a localized noise source [see, e.g.,(Godin *et al.*, 2010)]. Position of the additional peak depends on the bearing of the localized source relative to the line that connects the positions of the two receivers. The bearing was estimated for the 31 NCCFs used in this study and was found to be consistent with the bearing of the entrance to New York Harbor [Fig. 1(a)], where shipping lanes converge. This direction is appreciably different from but close to the direction from the HLA hydrophones to the SHRU.

III. PASSIVE NORMAL MODE EXTRACTION FROM THE NCCF IN A DYNAMIC ENVIRONMENT

A. Retrieving acoustic normal mode travel times by time warping

Time-warping transform in underwater acoustics is a single-hydrophone based modal filtering technique to extract dispersion curves of the received signal. The dispersion curve of mode m can be represented as a frequency-dependent travel time $t_m(f)$ or group speed $g_m(f)$ and time warping as a nonlinear signal processing method is dedicated to decomposing the modal features of a received signal in the low-frequency (<500 Hz) and shallow water

https://doi.org/10.1121/10.0006664

(<200 m) scenario (Bonnel *et al.*, 2020b). Time warping is to filter modes in theory (Le Touzé *et al.*, 2009), which is based on unitary transform in the time-frequency (TF) domain (Baraniuk and Jones, 1995). Time warping was introduced by Bonnel in the underwater acoustics community in 2010, and it has been applied to seabed characterization (Bonnel and Chapman, 2011; Zeng *et al.*, 2013; Dong *et al.*, 2016; Duan *et al.*, 2016; Bonnel *et al.*, 2019; Guarino *et al.*, 2021), estimates of the spatiotemporal variability of ocean sound speed (Ballard *et al.*, 2014), extraction of dispersion curves from NCCF (Zang *et al.*, 2015; Brown *et al.*, 2016; Sergeev *et al.*, 2017; Tan *et al.*, 2019; Tan *et al.*, 2020), etc. This ideal waveguide-based time-warping transform and its modified operator (Niu *et al.*, 2014), as well as the general warping transform (Brown, 2020), have been proven to be robust algorithms that incorporate the complexity of the ocean environment (Bonnel *et al.*, 2020b).

Time warping transforms a received broadband signal $S(\tau)$ into the "warped" signal

$$\tilde{S}(w(\tau)) = |dw(\tau)/d\tau|^{-1/2} S(\tau), \tag{2}$$

where τ and $w(\tau)$ represent time in the physical and warped domains, respectively. In the NI context, the signal $S(\tau)$ is the EGF retrieved from either P-NCCF or N-NCCF, with τ being the absolute value of the time delay in the NCCF (Tan *et al.*, 2019). Equation (2) combined with the warping function $w(\tau) = (\tau^2 - \tau_r^2)^{1/2}$ maps the received signal $S(\tau)$ through a nonlinear resampling process into $\tilde{S}(w(\tau))$ such that each modal component appears to be tonal in the warped domain. Here, $\tau_r = r/c_w$ represents the earliest arrival time of the received signal being warped, the choice of τ_r and the equivalent choice of sound speed in water c_w are selected empirically and discussed in Sec. III B. In the active scheme, r is the horizontal distance between source and receiver, whereas r in the context of NI is the distance between two receivers (the ith HLA hydrophone to the SHRU in Fig. 1). The inverse time-warping transform is the inversed version of Eq. (2) with $w^{-1}(\tau) = (\tau^2 + \tau_r^2)^{1/2}$ which restores the original signal $S(\tau)$ from the warped signal $\tilde{S}(w(\tau))$.

Due to the spurious arrival that occurred in P-NCCF, explained earlier in Sec. II E, we use measured N-NCCFs only as the signals to interrogate the environment. Then $S_i(\tau) = CF_i(-\tau)$, $\tau > 0$, $i = 1, 2, \ldots, 32$. In normal mode theory, each $S_i(\tau)$ can be written as the sum of its modes as $S_i(\tau) = \sum_{m=1}^{M} S_{i,m}(\tau)$. Figure 6(a) shows the signal of the first receiver-pair $S_1(\tau)$, and its spectrogram is shown in Fig. 6(b). Due to the interference between each consecutive mode of $S_{1,m}(\tau)$, it is not possible to identify individual mode contributions and therefore each modal dispersion curve cannot be retrieved from the spectrogram separately. However, after the time-warping transform, each modal

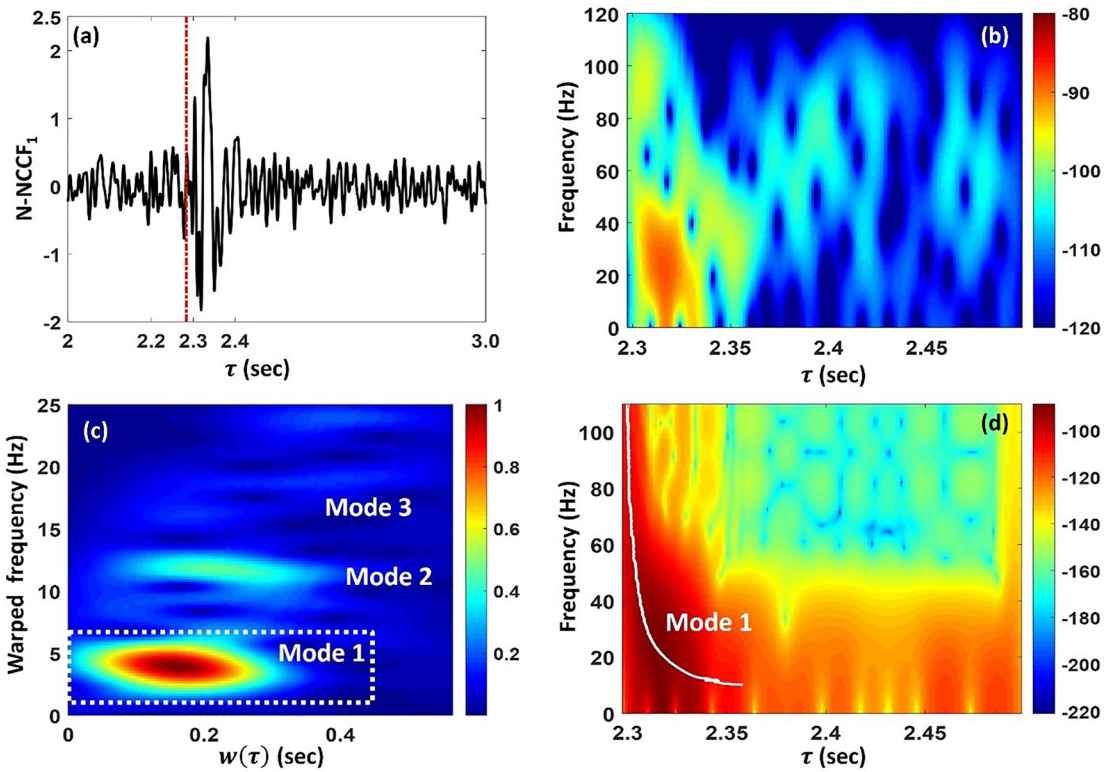

FIG. 6. (Color online) Application of the time-warping transform to separate normal-modal components of a measured NCCF and passively measure dispersion curves of the normal modes. (a) The N-NCCF$_1$ between the SHRU and the first HLA hydrophone, $S_1(\tau)$, serves as the input signal for time warping, with starting reference time $\tau_r \approx 2.28$ s shown as a vertical dashed-line. (b) Spectrogram of $S_1(\tau)$ is shown by color in dB relative to an arbitrary reference. (c) Spectrogram of the same N-NCCF$_1$ after time warping. Contributions of individual normal modes are separated. A time-frequency mask is applied to the area within the dashed-box to isolate mode 1 at the unwarping stage of signal processing. (d) Spectrogram of the waveform $S_{1,1}(\tau)$ after unwarping. The solid line shows the mode 1 dispersion curve $\tau_{1,1}(f)$ retrieved from the spectrogram.

component m occupies distinct frequency bands, and each modal energy is distinguishable in the spectrogram of the warped signal $\tilde{S}_{1,m}(w(\tau))$ as shown in Fig. 6(c).

To isolate a single mode m from $S_1(\tau)$, a TF mask is applied to the short-time Fourier transform of $\tilde{S}_1(w(\tau))$. This particular TF mask of mode 1 is illustrated in Fig. 6(c) to capture the energy of mode 1 excluding other modal energy. The inverse short-time Fourier transform of the result gives the isolated modal waveform in the warped domain as $\tilde{S}_{1,1}(w(\tau))$, after the modal selection process by the TF mask in Fig. 6(c). This single mode in the warped domain is then unwarped back to the physical domain as $S_{1,1}(\tau)$ by application of the inverse time-warping procedure. The spectrogram of this single mode $S_{1,1}(\tau)$ is illustrated in Fig. 6(d) without modal interference. The time-warping transform and its inverse is an energy conservation process, such that $\sum_{m=1}^{M} S_{i,m}^2(\tau) = \sum_{m=1}^{M} \tilde{S}_{i,m}^2(w(\tau))$. One of the advantages of the time-warping transform is that "noise," i.e., the energy which does not belong to any modal component of the signal (NCCF in this case), is filtered out in the warped domain by the selected TF masks [Fig. 6(c)]. For instance, the energy appearing in the warped domain between modes 1 and 2, which is represented by the relatively weak but nonzero background in the 6–9 Hz band in Fig. 6(c), is not brought back from $\tilde{S}_{1,1}(w(\tau))$ to $S_{1,1}(\tau)$.

In the spectrogram of a single-mode m of broadband waveform, the peak values with respect to time at any given frequency lie close to the travel time $\tau_{i,m}$, which corresponds to the modal group speed $g_{i,m}(f) = r_i/\tau_{i,m}(f)$ at that frequency bin f, with r_i as the horizontal distance from the ith HLA hydrophone to the SHRU [Fig. 1(b)]. The modal travel time of frequency $\tau_{i,m}(f)$ is extracted from the spectrogram using the reassignment process (Fulop and Fitz, 2006) with a high resolution estimate. The retrieved dispersion curve $\tau_{1,1}(f)$ of application of the reassignment process is illustrated in Fig. 6(d) for $S_{1,1}(\tau)$. This procedure was repeated, and the frequency dependence of the travel time $\tau_{i,m}(f)$ was determined for the first three modes using optimum, mode- and HLA hydrophone-specific TF masks for all 31 measured NCCFs. Non-overlapping 0.2 Hz bin width is used for modes 1, 2, and 3 in the 10–110, 30–110, and 45–110 Hz frequency bands, respectively. In Fig. 7(b), the frequency dependence of the path-averaged group speeds $\bar{g}_m(f)$ is an empirical average over $g_{i,m}(f)$ and is illustrated in two different acoustic observations (Fig. 2). The $\bar{g}_m(f)$ will be used as inputs for inverse problems in Sec. IV. Mode 3, $\tilde{S}_{1,3}$ has relatively less energy than the first two modes seen in Fig. 6(c), but the $\bar{g}_{m=3}(f)$ from the path-average still returns a reliable quality.

B. Selection of reference time τ_r in time warping based on minimum SSP

In the warping function $w(\tau)$, τ_r has the meaning of the earliest arrival time of the received signal being warped. For each receiver pair i, the best $\tau_{r,i}$ meets the condition that all modes are best separated and fully resolved in the warped domain spectrogram [Fig. 6(c)]. The optimum reference time for the first receiver pair $S_1(\tau)$ is $\tau_{r,1} = 2.28$ s; this reference time is shown as a vertical dashed line in Fig. 6(a). Since τ_r is defined as r/c_w and if the horizontal distance r is known and fixed, perturbing the optimum τ_r in Fig. 6(a), changes the correct arrival time of the received signal and thus also degrades the quality of modal separation shown in Fig. 6(c). For all 31 measured N-NCCFs, the selection of $\tau_{r,i}$ increases with the nominal horizontal distance r_i. Each $\tau_{r,i}$ is equal to r_i divided by an empirically chosen sound speed in water c_w, and this c_w is usually subjectively chosen from one value of measured SSP *in situ* (Bonnel *et al.*, 2020b). The theoretical choice of τ_r corresponds to the shortest mode travel time (at frequencies above the Airy frequency) as mentioned in Bonnel *et al.* (2017), but the relationship between r/τ_r and SSP has not been investigated.

Normal mode theory (Brekhovskikh and Godin, 1999) predicts that, in a range-independent waveguide with fluid

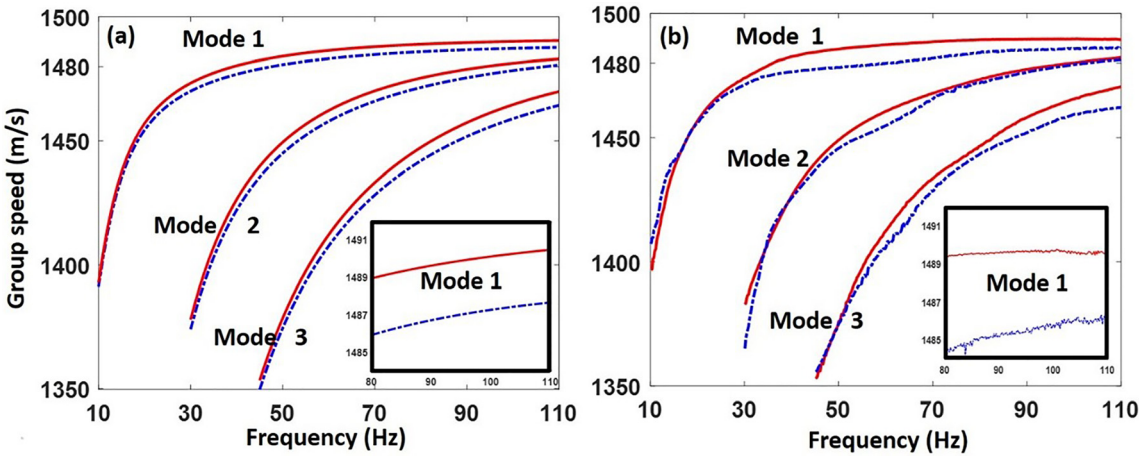

FIG. 7. (Color online) Dispersion curves (group speeds) of the first three normal modes in two different observation periods. (a) Synthetic group speeds $g_m(f)$ calculated using the sound speed profiles $C_1(z)$ (dashed lines) and $C_2(z)$ in Fig. 2(b) (solid lines) with seabed properties from Tan *et al.* (2020). A magnified portion of $g_1(f)$ in the higher-frequency band 80 Hz $< f <$ 110 Hz is illustrated in the insert to show the asymptotic region of Eq. (3). (b) Averaged measured group speeds $\bar{g}_m(f)$ from NCCF_1 (dashed lines) and NCCF_2 (solid lines).

https://doi.org/10.1121/10.0006664

bottom, the group speed $g_m(f)$ of each mode asymptotically approaches the minimum $C_{\min}$ of the SSP in water in the high-frequency limit,

$$\lim_{f\to\infty} g_m(f) = C_{\min}. \tag{3}$$

Hence, $C_{\min}$ is expected to approximate $c_w = r/\tau_r$. But how high the frequency f must be for $g_m(f)$ to approach $C_{\min}$ within a reasonable tolerance (say, 1 m/s) depends on the environment. At first glance, the approximation $c_w = C_{\min}$ will not fit in this NI scheme of a low-frequency (<110 Hz) noise in a shallow-water environment (Fig. 1). Figure 7(a) is a simulation of three modal dispersion curves in 10–110 Hz, to numerically demonstrate that Eq. (3) can be satisfied even in this scenario. The dispersion curves close to the Airy phase that cannot be measured accurately enough by the Eq. (2) based warping transform (Tan *et al.*, 2019; Bonnel *et al.*, 2020b) are not shown in Fig. 7. The fundamental mode m=1 is the earliest mode to asymptotically satisfy Eq. (3) compared with other higher-order modes as frequency increases. The dispersion curves in Fig. 7(a) are simulated based on the seabed properties inverted from the previous study at the same site (Tan *et al.*, 2020), with $C_1(z)$ and $C_2(z)$ as input SSPs from Fig. 2(b). In Fig. 7(a), the fundamental mode's group speed, $g_{m=1}(f)$ is the earliest mode to reach the asymptotic region of the $C_{1\min}$ and $C_{2\min}$ in Fig. 2(b), whereas at the highest frequency of 110 Hz, $g_{m=2}(f)$ and $g_{m=3}(f)$ are still far from the asymptotic region to satisfy Eq. (3) yet. In Fig. 2(b), the $C_{1\min}$ is 1487.9 m/s at z = 33 m, and $C_{2\min}$ is 1491.9 m/s at z = 40 m. Figure 7(a) simulation at 110 Hz returns $g_{m=1}(f)$=1487.8 m/s from $C_1(z)$ and 1490.7 m/s from $C_2(z)$, respectively, and is close to the expected $C_{1\min}$ and $C_{2\min}$ in Fig. 2(b). At 110 Hz, the $g_{m=1}(f)$ simulated from $C_1(z)$ is only 0.1 m/s less than the $C_{1\min}$ shown in Fig. 2(b). The $g_{m=1}(f)$ simulated from $C_2(z)$ at the same 110 Hz, however, returns a 1.2 m/s less than the expected $C_{2\min}$, which is a larger discrepancy. The physical clue to this larger discrepancy also lies in Fig. 2(b). First, the shape of SSP $C_1(z)$ leads $g_{m=1}(f)$ to a faster convergence (lower frequency bin required) to $C_{1\min}$ than to that in $C_{2\min}$, because the gradient (sound speed change with respect to water depth) above $C_{1\min}$ is larger than that of $C_{2\min}$. This larger gradient implies that group speed $g_{m=1}(f)$ will converge to $C_{1\min}$ faster as frequency increases. Therefore, $g_{m=1}(f)$ in $C_2(z)$ requires higher frequency than $C_1(z)$ to satisfy Eq. (3). When simulations are extended to the higher frequency of 150 Hz with $C_2(z)$, the discrepancy between the simulated $g_{m=1}(f = 150\,Hz)$ and $C_{2\min}$ decreases to 0.6 m/s, which is within the chosen tolerance. This discrepancy is smaller than the measurement errors discussed in Sec. IV B.

The $NCCF_2$ and its measured $C_2(z)$ were used in the previous study (Tan *et al.*, 2020) to invert seabed properties, where dispersion curves at the lower frequency band close to the Airy phase on the one hand are less sensitive to sound speed changing in the water column as seen both in the simulation [Fig. 7(a)] and the empirical result [Fig. 7(b)]. On the other hand, dispersion curves at the higher frequency band are more sensitive to sound speed change, and thus we can use the seabed properties inverted from $NCCF_2$ to retrieve the estimated $C_1(z)$ from $NCCF_1$ by matching dispersion curves.

C. Effect of temporal variability of the water column on group speeds of acoustic normal modes

Temporal variability of the water column has a significant effect on estimation of the NCCFs and retrieval of empiric Green's functions from these estimates (Godin, 2018). In this section, we quantify the effect of the observed temporal variability on acoustic fields in the 10–110 Hz frequency band discussed.

Variations of the two 15-day water column sound speeds with time are illustrated in Fig. 2(a). Here, Fig. 8 shows the average $C_1(z)$ and $C_2(z)$ with depth-dependent standard deviation $\pm\sigma$ of the sound speed during the 1st and 2nd acoustic observation periods. Figure 8(b) shows stronger temporal variability than Fig. 8(a) and stronger impact on group speeds of acoustic normal modes. Therefore, Fig. 8(b) is chosen for

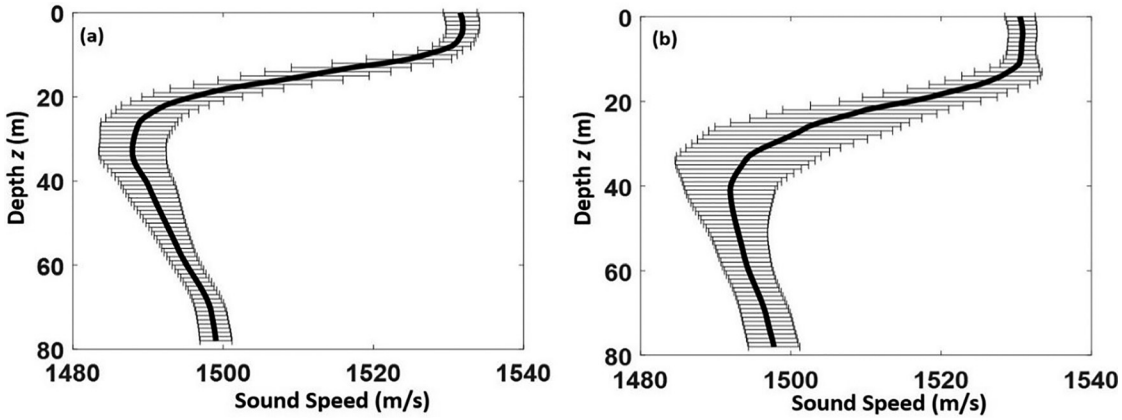

FIG. 8. Statistics of the water column variability in two 15-day observation periods. (a) The solid line shows the average sound speed profile $C_1(z)$ in the first observation period, with the standard deviation $\pm\sigma$ shown as error bars. The standard deviation is shown as error bars to the left and to the right of the mean value. (b) The same as shown in (a) but for the second observation period, with the solid line showing the average sound speed profile $C_2(z)$.

analysis in this section. The average $C_2(z)$ has the maximum of 1531.4 m/s at 4 m depth and the minimum of 1490.7 m/s at 37 m depth. The depth-averaged standard deviation is 5.55 m/s. The standard deviation has very large values of 10–13 m/s in the thermocline at depths 15–30 m, with the maximum of 13.2 m/s at 19 m depth.

Temporal variations of the normal mode travel times have been evaluated by modeling sound propagation in range-independent waveguides with the water-column SSPs obtained as 15 daily averages of the measured SSPs [Fig. 9(a)]. In these simulations, the water depth is 78 m and the geoacoustic parameters of the seabed are taken from the previous work (Tan *et al.*, 2020). Variations of the group speed are found to increase with frequency for all normal modes [Figs. 9(b) and 9(c)]. Mode 1 proves to be more sensitive to sound speed variations than modes 2 and 3, especially at lower frequencies. This is in contrast to bathymetry variations, where the higher-order modes have the higher sensitivity (Tan *et al.*, 2020). Under the conditions of the SW06 experiment, at frequencies above 60 Hz, temporal variations of the group speed become significant for all normal modes [Figs. 9(c)]. Figure 9(d) compares the group speeds in the average ocean with the average of group speeds over time and illustrates the nonlinearity of the perturbations induced by the temporal variations of the water column. (The difference between the two averages would be zero for linear perturbations.) The nonlinearity proves to be most pronounced for mode 1, where the nonlinearity rapidly increases with frequency. The nonlinearity illustrates the limits within which time averaging of acoustic observables can help to overcome temporal variability of the ocean. In the 10–110 Hz frequency band, the group speed nonlinearity remains smaller than the measurement errors on individual paths, which indicates applicability of time averaging. This finding is in agreement with the previous observations reported in Tan *et al.* (2020).

D. Effect of the horizontal inhomogeneity of the water column on travel times of acoustic normal modes

On diurnal and shorter time scales, water column variability at the SW06 site is dominated by tidally generated trains of NLIWs. NLIW-induced variations are not only time dependent, but also horizontally inhomogeneous as the wave trains travel across the SW06 site and have a complex internal structure. In this section, we characterize the effect of horizontal gradients of the sound speed on modal travel times. Sound propagation in horizontally inhomogeneous,

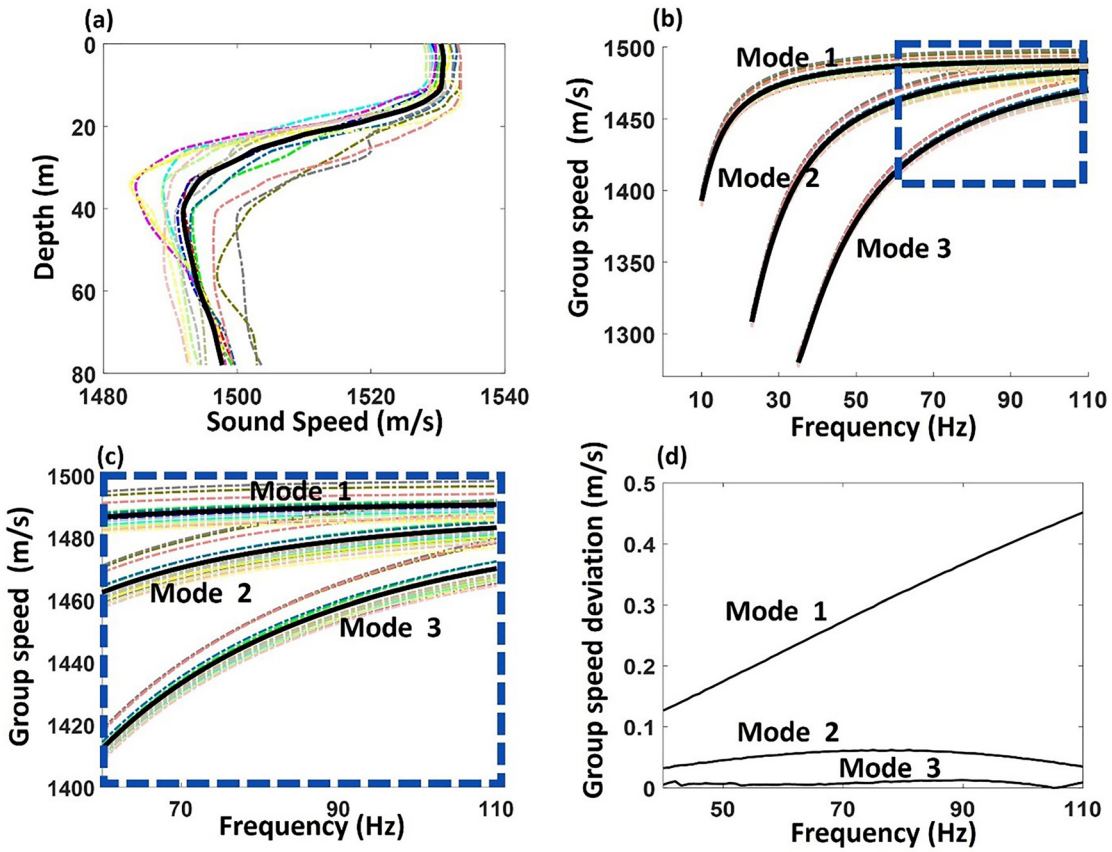

FIG. 9. (Color online) Simulation of the effects of temporal variability of the water column on modal group speeds. (a) Fifteen daily averages of measured SSPs are shown by dashed lines, with the 15-day average $C_2(z)$ shown by a solid line. (b) Dispersion curves of the first three normal modes in the range-independent oceans with different SSPs are shown with the same dashed lines as the corresponding SSPs in (a). (c) A detailed view of a part of (b) is shown in the 60–110 Hz frequency band, where the group speeds are more sensitive to SSP variations. (d) The absolute value of the difference between the group speed in the ocean with the 15-day average $C_2(z)$ and the average of the group speeds in each of the 15 days is shown for the first three normal modes.

https://doi.org/10.1121/10.0006664

time-dependent ocean is modeled within the adiabatic (Godin *et al.*, 2006; Godin *et al.*, 2019) and frozen medium (Godin *et al.*, 2006) approximations disregarding horizontal refraction.

To a good approximation, dependence of the temperature and sound speed in an NLIW on horizontal coordinates and time can be modeled as a plane wave propagating from the shelf break to the shore (Godin *et al.*, 2006; Newhall *et al.*, 2007; Tang *et al.*, 2007). Then, SSP measurements obtained with a single thermistor chain (Fig. 2) are sufficient to model the entire sound speed field.

We choose the path between the HLA hydrophone #32 and the SHRU to model sound propagation in a horizontally inhomogeneous environment. The hydrophone is the closest of the HLA hydrophones to the thermistor chain, and the NLIW propagation direction is close to the direction from the hydrophone to the SHRU (Newhall *et al.*, 2007; Tang *et al.*, 2007). The length of the propagation path is about 3830 m. Traveling from the hydrophone #32 to the SHRU at the speed of 0.9 m/s, the NLIW covers this distance in about 1.2 h. Within the plane wave approximation for NLIW, horizontal gradients of the sound speed are its scaled time derivatives. To find the largest horizontal gradients, we identified the time period in the measurements of the 2nd observation period with the strongest variability during any 1.2-h period. The strongest short-time variability is found on the Julian day 235 (August 22) after about GMT 06:00 [Fig. 10(a)], with the average SSP and its standard deviation $\pm\sigma$ during the 1.2-h period shown in Fig. 10(b). Quasi-periodic variations of the sound speed in the thermocline in Fig. 10(a) are characteristic of the passage of the individual internal wave solitons, which comprise the NLIW, past the thermistor chain (Newhall *et al.*, 2007; Tang *et al.*, 2007). The peak-to-trough magnitude of these variations reaches 30 m/s. SSP measurements in the vicinity of the HLA hydrophone #32 and the speed of NLIW propagation are used to model a range-dependent sound speed field on the propagation path to the SHRU at the time of strongest range dependence (GMT 07:12 on the Julian day 235) when the NLIW train occupies the entire propagation path [Figs. 10(c) and 10(d)].

The results of modeling mode travel times in the range-dependent environments described previously are presented in Figs. 10(c) and 10(d) in terms of the effective group

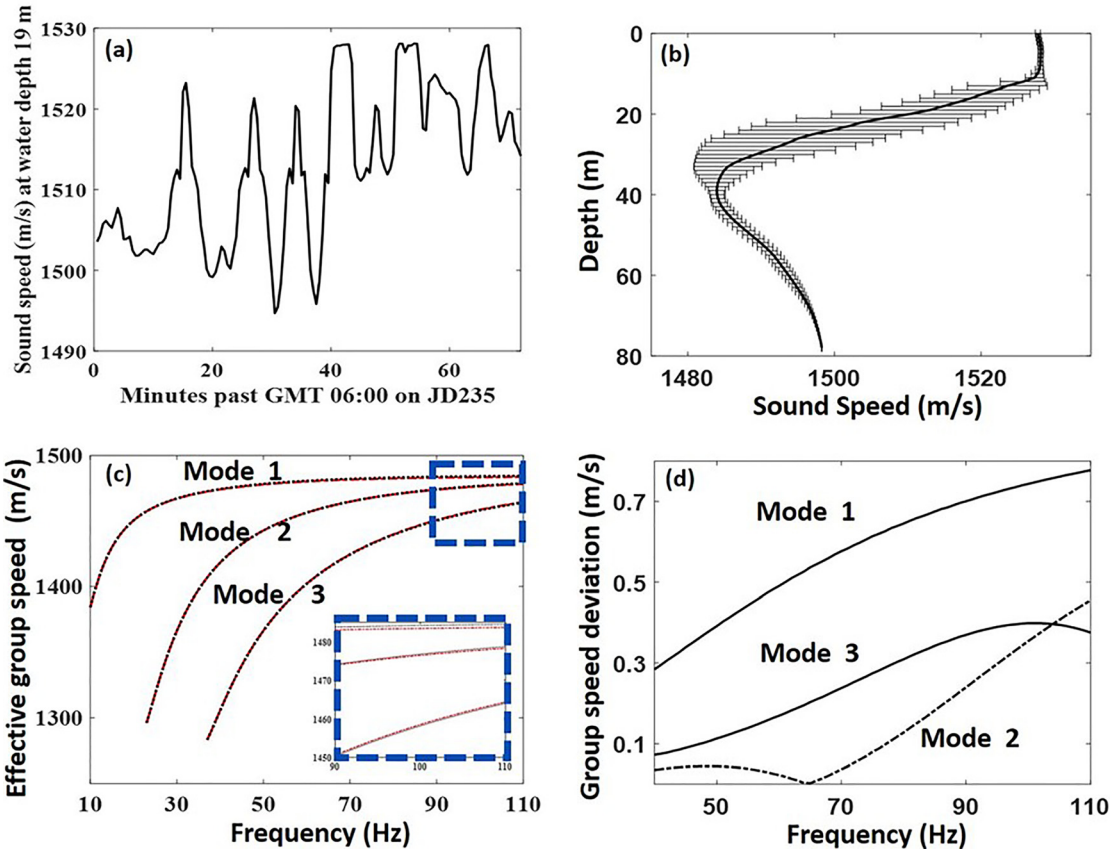

FIG. 10. (Color online) Simulation of the effects of the water column range dependence on modal travel times. (a) Measured time dependence of the sound speed at 19 m depth during the period of the highest observed water column variability. (b) The average SSP (solid line) and its depth-dependent standard deviation $\pm\sigma$ during the 1.2 h period shown in (a). The standard deviation is shown as error bars to the left and to the right of the mean value. (c) Effective group speeds of the modes 1–3 calculated as the ratio of the propagation range to the mode travel time in the range-dependent environment (dashed lines) and group speeds of the modes in the range-independent environment with the average SSP (dotted lines). The insert shows a blow-up of the boxed part of the main plot in the 90–110 Hz frequency band. The modeled range-dependent environment occurs when the NLIW train with the sound speed variation illustrated in (a) and (b) occupies the entire propagation path. (d) The absolute value of the difference between the normal mode group speeds in the range-independent ocean and the effective group speeds shown in (c).

speed. The latter is defined as the ratio of the propagation range to the mode travel time between the HLA hydrophone #32 and the SHRU. In these simulations, as in Sec. III C, water depth is 78 m and the geoacoustic parameters of the seabed are taken to be equal to those of the optimal geoacoustic model in Tan *et al.* (2020). Even in the case of the strongest expected range-dependence of the sound speed, the differences between the mode travel times in range-dependent and range-independent ocean are found to remain within the measurement errors (see Sec. IV) of the modal travel times on individual paths [Fig. 10(d)]. The results presented in Fig. 10(d) characterize the upper bound of the errors due to SSP range dependence. With the periods of strong range-dependence due to the NLIW trains occupying only a fraction of the observation time, the actual effects of the SSP range dependence are expected to be significantly reduced compared with the values in Fig. 10(d).

Since the effects of the water column range dependence on mode travel times (just as the effects of bathymetry range dependence, which are considered in Sec. IV) are smaller than the measurement errors on individual paths, with the data available, the advantages of measurement error suppression by path averaging far outweigh any possible benefits of including range dependence in geoacoustic and SSP inversions.

IV. THE INVERSE PROBLEM OF SSP RETRIEVAL

The $NCCF_1$/$NCCF_2$ and their corresponding modal dispersion curves contain environmental information including geoacoustic parameters of seabed GM_1/GM_2 and time-averaged SSPs $C_1(z)$/$C_2(z)$. See Table I for a list of notations. The GM_1 and GM_2 represent the seabed properties and are supposed to remain unchanged within a half-month timeframe such that $GM_1 \approx GM_2$. What causes the difference between retrieved group speeds shown in Fig. 7(b) is the difference between $C_1(z)$ and $C_2(z)$. The Appendix discusses the geoacoustic inversion process to retrieve GM_1 from $NCCF_1$ with the measured $C_1(z)$ assumed known. This retrieved GM_1 and the previous retrieved GM_2 (Tan *et al.*, 2020) are largely consistent and the error bounds are within reasonable tolerance and alternatively demonstrate the robustness of NCCFs, even retrieved in the dynamic environment. The dispersion curves extracted from $NCCF_1$/$NCCF_2$ are different because of the sub-seasonal, temporal sound speed variability in the water column between $C_1(z)$ and $C_2(z)$. Using these consistent geoacoustic properties, Sec. IV A describes the parameterization of SSP to restore the time-averaged $C_1(z)$ from $C_2(z)$, and Sec. IV B describes retrieval of $C_1(z)$ by matching dispersion curves using the previously obtained GM_2 as the seafloor model.

A. Parameterization of SSP: Empirical orthogonal function (EOF)

The measurement of 30-d' SSPs was described in Sec. II B. The differences of measured sound speeds are spatio-temporally significant in Figs. 2 and 8, and are particularly observable in the thermocline layer $z = 15$–40 m. The sound speed variability of the 2nd observation period is more dynamic than the 1st observation in Fig. 2(a). Solution of the inverse problem of passive acoustic characterization of the water column properties requires that the unknown SSPs are described by a finite and preferably small set of parameters. This section describes the choice and properties of SSP representation that we use to solve the inverse problem.

Three types of SSP representation have been considered: orthogonal polynomials, affinity transformation, and EOFs. With the first technique, Legendre polynomials served as a simple orthogonal basis to represent water-column SSP in the range $0 < z < 82$ m. With the second technique, water column is split into three layers: from the ocean surface to the bottom of the mixed layer, from the bottom of the mixed layer to the sound speed minimum, and from the sound speed minimum to the seafloor. The positions of the sound speed minimum and the extent of the mixed layer are not fixed. In each of the three layers, $c(z)$ is modeled as an affinity transform (Snapper and Troyer, 2014) in the c–z plane of the known SSP $C_2(z)$ in the respective layer. Conditions of continuity of the sound speed and its gradient are imposed at the boundaries of the middle layer. The third technique uses a data-derived orthogonal basis of EOFs, which are described in more detail in the following.

When applied to approximating SSP $C_1(z)$, the affinity transformation technique returns the largest root mean square error (RMSE) compared to the error the Legendre polynomials and EOFs with the same number of free parameters have in representing $C_1(z) - C_2(z)$. The first six Legendre polynomials return a RMSE of 1.7 m/s in approximating $C_1(z) - C_2(z)$, which is considerably larger than the error of the approximation with six EOFs. Based on these results, we conclude that the EOF-based representation is most suitable for the inverse problem at hand.

EOFs are commonly used to describe the structure of SSP in underwater acoustics (Huang *et al.*, 2008; Jiang and Chapman, 2009). The model representing the unknown SSP, $c(z)$, is as an expansion of EOFs:$c(z) = c_0 + \sum_{j=1}^{J} \alpha_j \cdot E_j(z)$, where c_0 is the average SSP that serves as a reference and J is the total number of orthogonal functions, α_j is the amplitude coefficient, and $E_j(z)$ is the EOF basis. Ideally, $c(z)$ can be perfectly restored when the number of basis J approaches infinity. This is termed empirical because it is constructed completely from the statistically measured data, and each $E_j(z)$ is the eigenvector decomposed from the covariance matrix of space-time measured SSPs. This work aims to passively restore $C_1(z)$ in terms of the finite number of EOFs, which are derived from *in situ* measurements during the second observation period [the solid box in Fig. 2(a)] by finding the corresponding coefficients such that the RMSE of $|C_1(z) - c(z)|$ is minimized *via* matching dispersion curves. A MATLAB-based singular variable decomposition (SVD) algorithm is applied to these space-time SSPs of water depth 82 m and a 30-s interval matrix for eigen-decomposition to obtain the EOFs, and the linear combination of these data-

https://doi.org/10.1121/10.0006664

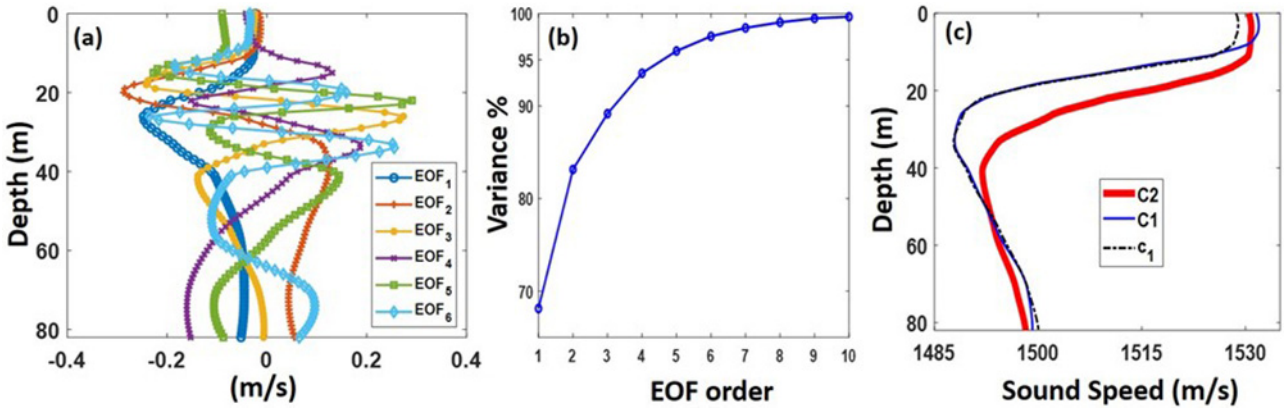

FIG. 11. (Color online) SSP restoration based on the EOFs that are obtained from the SSPs measured during the second observation period. (a) The first six EOFs. (b) Cumulative variance percentage increase with the number of EOFs used. (c) Measured SSPs $C_1(z)$ (thin line) and $C_2(z)$ (thick line) and the restored SSP $c_1(z)$ (dashed line), which is the approximation of $C_1(z)$ obtained using Eq. (4).

driven EOFs can invert the $C_1(z)$ by minimizing the following cost function:

$$\kappa_1(\boldsymbol{\alpha}) = \sqrt{\frac{1}{D}\int_{z=0}^{D}\left[C_1(z) - c(z)\right]^2 dz},$$
$$c(z) = C_2(z) + \sum_{j=1}^{J} \alpha_j \cdot E_j(z). \tag{4}$$

Here, water depth $D = 82$ m, and $C_2(z)$ is a reference SSP. $\boldsymbol{\alpha} = [\alpha_1, .., \alpha_J]$ are the unknown amplitude coefficients to be retrieved in the inverse process, and $\mathbf{E}(z) = [E_1(z); \ldots; E_J(z)]$ are the EOF bases used to minimize Eq. (4) with orthogonal properties between each E_j. For later comparison purposes, the restored SSP using Eq. (4) is abbreviated as $c_1(z)$. Here, $J = 6$ is the total number of EOFs used to obtain an approximation $c_1(z)$ of $C_1(z)$.

Figure 11(a) illustrates the first six EOFs; each $E_j(z)$ is normalized by $\int_{z=0}^{D} E_j^2(z)\,dz = 1$ and the variance is represented by taking the square of each EOF's corresponding singular value (eigenvalue). The first six EOFs comprise 97.5% of total variance [Fig. 11(b)], which are sufficient to restore $C_1(z)$ to $c_1(z)$ as illustrated in Fig. 11(c). The inverted $\boldsymbol{\alpha} = [51.1, 44.8, 11.6, -13.3, 1.4, 3.4]$ retrieved from Eq. (4) is listed in Table II for later comparison purposes. MATLAB-based genetic algorithm is applied to retrieve $\boldsymbol{\alpha}$, and the result converges to the analytic solution of orthogonal basis rapidly. An EOF order higher than $J = 6$ brings a trivial improvement to the restored $c_1(z)$ in Fig. 11(c), therefore, $J \geq 7$ is not considered to avoid an unnecessary burden on the later inverse process of matching dispersion curves.

The restored $c_1(z)$ and measured $C_1(z)$ are almost perfectly matched except at the mixed layer $z = 0$–15 m, with about a 3 m/s sound speed discrepancy [Fig. 11(c)]. This is because the first two temperature sensors attached on the VLA were either lost or ineffective during the experiment, please see Table 30 of Newhall *et al.* (2007), and the SSPs at the mixed layer were estimated from other nearby sensors. In the previous SW06 studies (Huang *et al.*, 2008; Jiang and Chapman, 2008) close to the HLA-SHRU site (Fig. 1), the measured SSPs have almost constant values$\sim$1532 m/s from 0–10 m at the mixed layer. The total nine sensors of the VLA span the water column, were located at nominal depths of 15, 19, 22, 26, 34, 41, 56, 71, and 79 m, and were successful in measuring the depth-dependent sound speeds during the entire experiment. The SSPs presented in this work were interpolated with a one-meter resolution. Unfortunately, this 3 m/s discrepancy at the mixed layer $z = 0$–15 m casts an overall depth-average RMSE 1.0 m/s between $C_1(z)$ and $c_1(z)$ in Fig. 11(c). This 1.0 m/s RMSE due to parameterization slightly affects the inverse problem of matching dispersion curves in the next subsection, and its impact on experimental data will be quantified. In Eq. (4), if the starting depth $z = 0$ m is replaced with $z = 15$ m omitting the estimated SSP from nearby sensors at the mixed layer, the RMSE of $|C_1(z) - c_I(z)|$ significantly reduces from 1.0 m/s ($z = 0$–82 m) to 0.16 m/s ($z = 15$–82 m) when the same EOF order $J = 6$ is used. The EOFs are decomposed from the variability of the 2nd observation period, where most variabilities at the thermocline region ($z = 15$–40 m) are influenced by the diurnal NLIW, which deforms the SSP to move the particles up and down. It is conceivable that the sound speed at the

TABLE II. Summary of EOF amplitudes α_j obtained in different inversions for $C_1(z)$.

Cost functions	Approach	Restored SSP	α_1	α_2	α_3	α_4	α_5	α_6
κ_1, Eq. (4)	Matching the sound speed profile	$c_1(z)$ Fig. 11(c)	51.1	48.8	11.6	−13.3	1.4	3.4
κ_2, Eq. (5)	Matching synthetic dispersion curves $g_m(f)$	$c_2(z)$ Fig. 12(c)	51.0	47.0	15.0	−16.0	6.0	8.0
κ_3, Eq. (6)	Matching measured dispersion curves $\bar{g}_m(f)$	$c_3(z)$ Fig. 13(d)	54.0	42.0	12.6	−18.6	−5.7	3.2

mixed layer remains unchanged under the influence of the NLIW. In contrast to the thermocline ($z = 15$–40 m), the sound speed change in the mixed layer ($z = 0$–15 m) is much smaller, which results from the small change in the surface temperature over a 15-day period. Therefore, this small contribution to variabilities is not described by the first couple of EOFs [Fig. 11(a)], which are employed to capture the bigger change of variance at thermocline influenced by the NLIW.

B. Passive $C_1(z)$ inversion by matching dispersion curves

1. Benchmark simulation

To demonstrate that $C_1(z)$ can be retrieved *via* matching dispersion curves, an auxiliary procedure with a replica g_m was used to minimize the cost function κ_2 as

$$\kappa_2(\boldsymbol{\alpha}) = \sqrt{\sum_{m=1}^{M} \frac{1}{M \times N_m} \sum_{n=1}^{N_m} \left[g_m(f_n, C_1) - \widehat{g}_m(f_n, \boldsymbol{\alpha}) \right]^2},$$
$$c(z) = C_2(z) + \sum_{j=1}^{J} \alpha_j \cdot E_j(z). \tag{5}$$

Here, Eq. (5) is to minimize the mismatch of dispersion curves between the replica g_m and the forward modeling $\widehat{g}_m$. The previous passively inverted geoacoustic (seabed) properties GM_2 from $NCCF_2$ in Table III of the Appendix are used in g_m and $\widehat{g}_m$ as a model during the inversion. The inverse problem is to seek the best six coefficients α_j as a vector $\boldsymbol{\alpha}$ corresponding to $\boldsymbol{E}(z)$ to minimize the cost function κ_2 in Eq. (5) and thus retrieve the $c_2(z) \approx C_1(z)$ for all z. Equation (5) was run by MATLAB genetic algorithm until the improvement of κ_2 fell below 10^{-3} m/s.

The retrieved $\boldsymbol{\alpha}$ from Eq. (5) representing $c_2(z)$ is [51, 47, 15, –16, 6, 8] listed in Table II. The sensitivities to $\boldsymbol{\alpha}$ are shown in Fig. 12(a). Here, α_1 corresponding to the first coefficient of the fundamental basis EOF_1 [Fig. 11(a)] returns with the highest sensitivity and α_1 as the largest absolute value among all $\boldsymbol{\alpha}$, to seize the SSP change from $C_2(z)$ to $C_1(z)$, particularly in the thermocline region during the two distinct acoustic observation periods [Fig. 12(c)]. In Table II, the $\boldsymbol{\alpha}$ vector forming $c_2(z)$ from Eq. (5) is close to the exact solution from Eq. (4), and this retrieved $c_2(z)$ plotted in Fig. 12(c) is very close to $c_1(z)$ in Fig. 11(c). This confirms that matching dispersion curves to retrieve SSP is a viable approach.

Figure 12(b) investigates the relationship between RMSE of $|g_m - \widehat{g}_m|$ on the y axis and RMSE of $|C_1(z) - c(z)|$ on the x axis during the inversion process of Eq. (5), whereas $C_1(z)$ is taken as a ground truth. The parametrization error caused by matching synthetic dispersion curves g_m in Eq. (5) is 0.05 m/s, which is the minimum value of Eq. (5) shown in Fig. 12(b), and it corresponds to the RMSE of $|C_1(z)\text{-}c_2(z)|$ =1.36 m/s for the SSP mismatch. This 1.36 m/s RMSE in SSP spanning the full water column $z = 0$–82 m is slightly larger than the 1.0 m/s parameterization RMSE stated in Sec. IV A due to the missing sensors at the mixed layer $z = 0$–15 m during the experiment. If considering only water depth $z = 15$–82 m, where measured data of sound speeds exist, the RMSE of $|C_1(z) - c_2(z)|$ shrinks to 0.7 m/s, about half the value of 1.36 m/s as shown in Fig. 12(b), which is consistent with most errors resulting from sound speed mismatching at the mixed layer as mentioned in Sec. IV A. The comparison results of using $z = 0$–82 m and $z = 15$–82 m in RMSE of $|C_1(z) - c(z)|$ in Fig. 12(b) indicate that the dispersion curves are insensitive to the sound speed variation in the mixed layer. Also, in a simulation using $C_1(z)$ and $c_2(z)$, where about 3 m/s discrepancy exists in the mixed layer, the corresponding simulated dispersion curves from KRAKEN (Porter, 1992) return a maximum discrepancy of about 0.2 m/s among all modes and the overall depth average RMSE would be much smaller. This also suggests that the sound speeds in the mixed layer cannot be retrieved well due to insensitivity in dispersion curves at this 10–110 Hz frequency band, and the strong variability of sound speed change in the thermocline dominates the dispersion curves features shown in Fig. 7 with two distinct SSPs input, $C_1(z)$ and $C_2(z)$.

This small 0.05 m/s parametrization error in dispersion curves from the Eq. (5) simulation will be carried over while matching the actual empirically measured dispersion curves $\bar{g}_m$ in the next sub-section and the anticipated RMSE in the SSP difference will be $\geq$1.36 m/s due to the most errors resulting from the mismatch in the mixed layer.

2. Retrieving $C_1(z)$ from $NCCF_1$

The ultimate goal is to invert for an estimate of $C_1(z)$ from $NCCF_1$ and to approximate its value as $c_3(z)$ by

TABLE III. Geoacoustic models GM_1 and GM_2 derived from $NCCF_1$ and $NCCF_2$, respectively.

Parameter	Unit	GM_1 search bounds	Step	GM_1 / GM_2 optimum values	GM_1 / GM_2 error bounds[a]
Δr	m	[−10, 10]	0.1	8.9 / 5.6	–/[3.4, 6.6]
D	m	[75, 85]	0.1	83.1 / 82.0	[82.5, 84.8] / [81.0, 82.9]
H	m	[1, 30]	0.1	9.7 / 13.4	[7.4, 17.2] / [12.3, 17.4]
c_s	m/s	[1500, 1700]	1	1644 / 1624	[1631, 1697] / [1612, 1651]
ρ_s	–	[1.0, 2.2]	0.01	1.22 / 1.36	[1.15, 1.64] / [1.21, 1.49]
c_b	m/s	[1600, 2300]	1	1926 / 2058	[1858, 2059] / [2006, 2135]
ρ_b	–	[1.3, 3.0]	0.01	2.46 / 2.52	[2.18, 2.89] / [2.31, 2.72]

[a]GM_2 inversion results, including error bounds, are taken from Tan *et al.* (2020).

https://doi.org/10.1121/10.0006664

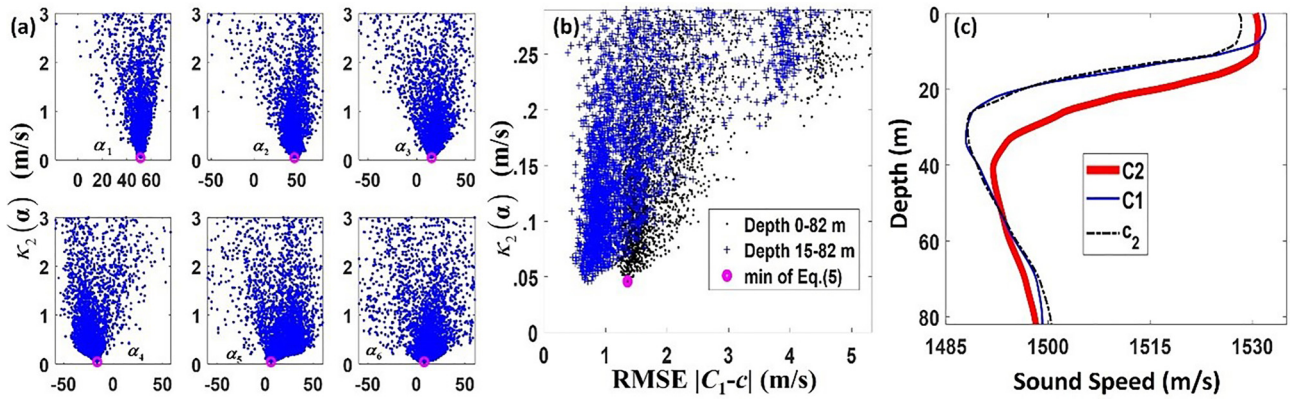

FIG. 12. (Color online) SSP inversion by matching synthetic dispersion curves. (a) Sensitivity of the cost function $\kappa_2(\boldsymbol{\alpha})$ Eq. (5) to EOF amplitudes α_j. In each panel, the cost function is plotted as a function of a single search parameter for the values of the other five parameters that were encountered during the optimization process. The thick circle indicates the position of the global minimum of 0.05 m/s of the cost function. Values of κ_2 up to 3 m/s are shown. (b) The relationship between the RMSE κ_2 in matching the dispersion curves and RMSE in matching the SSPs. The data points shown with dots and crosses refer to the sound speed RMSE calculated in the entire water column $0 < z < 82$ m and at depths of 15 m $< z <$ 82 m, respectively. (c) Comparison of the reference SSP $C_2(z)$ (thick line), ground-truth SSP $C_1(z)$ (thin line), and the restored SSP $c_2(z)$ (dashed line).

substituting empirical $\bar{g}_m$ for synthetic g_m in Eq. (5), in which case the cost function becomes

$$\kappa_3(\boldsymbol{\alpha}) = \sqrt{\sum_{m=1}^{M} \frac{1}{M \times N_m} \sum_{n=1}^{N_m} \left[\bar{g}_m(f_n) - \hat{g}_m(f_n, \boldsymbol{\alpha})\right]^2},$$

$$c(z) = C_2(z) + \sum_{j=1}^{J} \alpha_j \cdot E_j(z). \tag{6}$$

The $\bar{g}_m$ is an average value measured from the $NCCF_1$ through the time warping in Sec. III A. The $\hat{g}_m(f_n, \boldsymbol{\alpha})$ is modeled group speeds of normal modes from KRAKEN using the geoacoustic model GM_2 (Tan *et al.*, 2020), and $\boldsymbol{\alpha} = [\alpha_1, .., \alpha_J]$ are the unknown amplitude coefficients to be retrieved in the inverse process with $J=6$. The best fit $\hat{g}_m$ found *via* genetic algorithm and passively measured $\bar{g}_m$ are plotted in Fig. 13(a).

The group speeds $\bar{g}_m$, which are the input data for the inversion in Eq. (6), are known to within measurement errors. With 31 pairs of receivers, in each frequency bin, we have 31 measurements of the group speed of an individual normal mode. The measurement error is estimated as the square root of the unbiased sample variance of the 31 measurements. It is shown in Fig. 13(a) by vertical error bars (one standard deviation $\pm\sigma$) for each mode and for selected frequency bins and is discussed later.

Minimization of the cost function $\kappa_3(\alpha)$ returns a global minimum of 2.1 m/s in RMSE of the group speeds, which is illustrated in Fig. 13(b) and each subpanel of Fig. 13(c), where sensitivity of the cost function to each α_j is shown. This global minimum value is 0.75 and 0.4 m/s in an RMS larger than that in the previous work retrieving geoacoustic parameters GM_2 and GM_1 (see the Appendix), respectively. This relatively larger discrepancy in retrieving $c_3(z)$ is due to the following three reasons:

(1) The amplitude contrast between the regular, deterministic and irregular, random features of $NCCF_1$ is inferior to that of $NCCF_2$. Therefore, the quality of $\bar{g}_m(f_n)$ after modal extraction from Sec. III A is also inferior, especially for higher-order mode. Here, mode $m = 3$ accounts for the largest measurement errors [Fig. 13(a)]. The RMSE in the measurement of path-averaged modal group speeds is 0.245 m/s (Tan *et al.*, 2020) for $NCCF_2$ and 0.265 m/s for $NCCF_1$, respectively, with the same selected frequency bins.
(2) The modeling errors carried from the first stage retrieving the geoacoustic properties of seabed GM_2 to model the group speeds of normal modes $\hat{g}_m$ in Eq. (6).
(3) The 0.05 m/s parametrization RMSE in matching dispersion curves from Eq. (5).

The retrieved $\boldsymbol{\alpha}$ from Eq. (6) are [54.0, 42.0, 12.6, −18.6, −5.7, 3.2] listed in Table II with search bound [−100, 100] for each α_j [Fig. 13(c)] to invert for $c_3(z)$ [Fig. 13(d)]. The first two amplitudes α_1 and α_2, which account for most variance, are consistent with the results from Eq. (5), and the higher-order amplitudes α_4 and α_5 account for the most discrepancies in RMSE of $|C_1(z) - c_3(z)| = 1.48$ m/s [Fig. 13(b)] compared with the RMSE of $|C_1(z) - c_2(z)| = 1.36$ m/s [Fig. 12(b)] from Eq. (5) with synthetic data.

During the genetic algorithm-based SSP inversion process based on the cost function κ_3 Eq. (6), we have imposed two additional constraints:

(1) admissible SSPs have a single local minimum,
(2) $c(z) \geq 1485$ m/s for all z.

The constraints are motivated by oceanographic and physical considerations. The first one reflects the properties of SSPs measured during the second observation period [Figs. 2 and 9(a)] and is used to construct the EOF basis. The average SSP $C_2(z)$ and most of the individual measured SSPs exhibit a large, steady drop in the sound speed in the thermocline below the mixed layer, leading to a single SSP minimum. Nonlinear internal waves result in strong variations of the thermocline extent and depth of the SSP minimum [Figs. 2] but normally do not create additional local

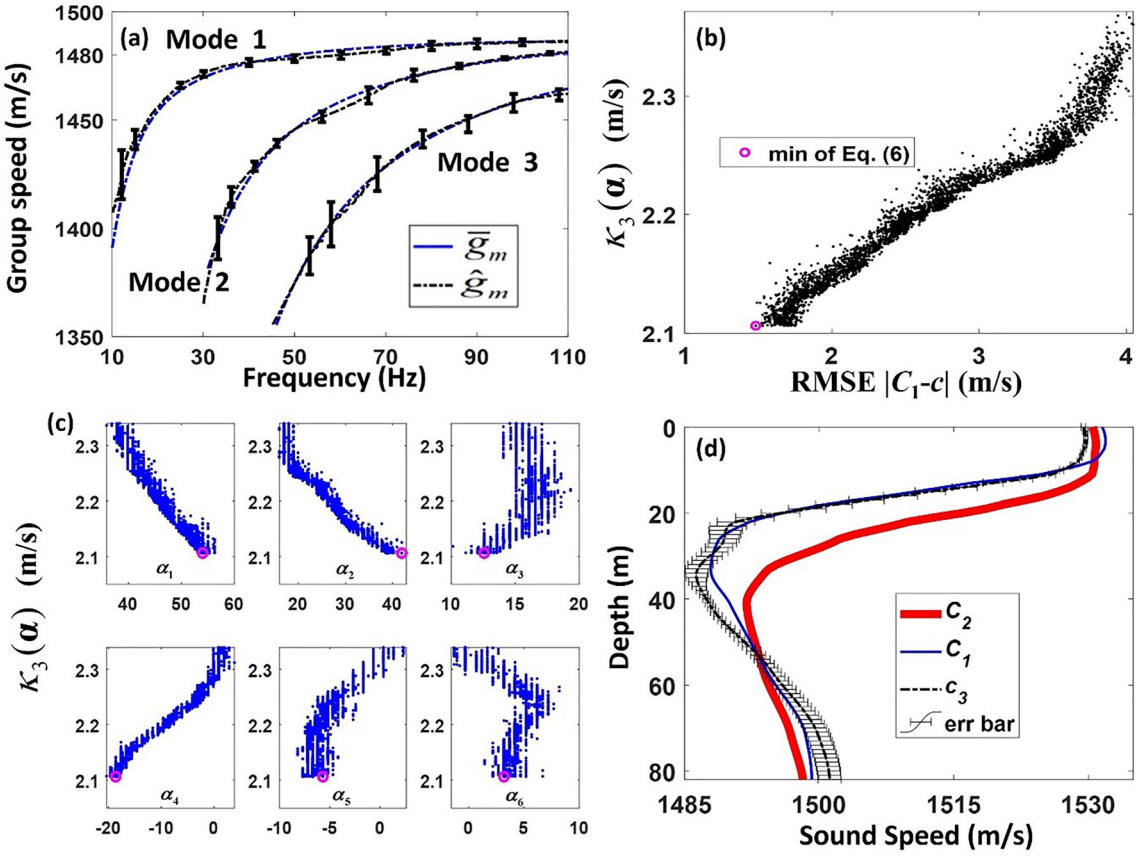

FIG. 13. (Color online) SSP inversion by matching measured dispersion curves. (a) Measured ($\bar{g}_m$, shown by solid lines) and best fit theoretical ($\hat{g}_m$, dashed lines) group speeds of normal modes. Vertical error bars show rms measurement errors for selected frequency bins. (b) The relationship between rms mismatch in the modal group speeds, κ_3 of Eq. (6), and the rms deviation of the sound speed profile from $C_1(z)$ during the inversion process after imposing the two physical constraints. The global minimum of 2.1 m/s of the cost function $\kappa_3(\alpha)$ is shown by a thick circle. (c) Sensitivity of the dispersion curve mismatch to each of the unknown parameters α_j. Values of κ_3 are shown up to one standard deviation of the measurement errors above the global minimum. (d) Comparison of the reference SSP $C_2(z)$ (thick line), ground-truth SSP $C_1(z)$ (thin line), and the retrieved SSP $c_3(z)$ (dashed line with error bars).

SSP maxima and minima. In the course of inversion, the first constraint helps to exclude unphysical candidate SSPs $c(z)$ in Eq. (6) and suppress the intrinsic ambiguity of the inversion of imperfectly measured data.

The second constraint originates from the physics of the normal mode dispersion. We impose a linear constraint of $c(z) \geq 1485$ m/s for all z in Eq. (6) during the inversion process. This condition is based on the passively measured value $\bar{g}_1(f_{\max}) = 1487.9$ m/s [Fig. 7(b)] and the finding in Sec. III B that the group speed of mode 1 will asymptotically approach the SSP minimum from below in the high-frequency portion of the data. The chosen lower bound of admissible $c(z)$ is set somewhat below $\bar{g}_1(f_{\max})$ to account for possible measurement errors. The actual retrieved minimum of $c_3(z)$ is 1486.3 m/s within a reasonable tolerance of $\bar{g}_1(f_{\max})$. This constraint effectively puts more weight on the higher-frequency portions during the inversion process where dispersion curves are more sensitive to the water column variability such that the $\bar{g}_m$ and $\hat{g}_m$ are better matched for higher-frequency bins close to 110 Hz for all modes shown in Fig. 13(a) compared with the previous work [Fig. 3(b) of Tan *et al.* (2020)]. On the contrary, geoacoustic inversions (Tan *et al.*, 2020) are more sensitive to the lower-frequency portions of the dispersion curves, which are more strongly affected by seabed properties due to deeper sound penetration below the seafloor.

Neither of the constraints use any quantitative, *a priori* environmental information. The constraints eliminate many unphysical possibilities of inverted SSPs and help to ensure that the value of RMSE of $|C_1(z) - c(z)|$ decreases monotonically as the value of the cost function $\kappa_3(\alpha)$ of Eq. (6) decreases during the inversion process [see Fig. 13(b)].

V. DISCUSSION

To estimate the uncertainty of the inversion results, we use the root-mean-square (rms) measurement error of modal group speeds as the scale of deviations of the cost function κ_3 [Eq. (6)] from its minimum value. The rms error of passive measurements of the modal group speeds is 0.265 m/s in the first observation period, as discussed in Sec. IV B 2. The SSPs, which result in the cost function κ_3 between its global minimum of 2.10 m/s and 2.365 m/s [Figs. 13(b) and 13(c)], provide admissible solutions of the inverse problem and collectively represent the uncertainty of the optimal solution $c_3(z)$ [Fig. 13(d)].

https://doi.org/10.1121/10.0006664

Results of the passive sound speed inversion should be compared to the ground truth, which is represented by contact measurements during the same observation period. In the admissible range of κ_3, the rms deviation of the inversion results from the average of the contact measurements, $C_1(z)$, varies in the range of 1.48–4.05 m/s [Fig. 13(b)]. The rms SSP deviation is calculated for every value of the vector $\boldsymbol{\alpha}$ that gives $\kappa_3 < 2.365$ m/s and is encountered during the genetic algorithm-based inversion process with the two physical constraints (Sec. IV B 2) imposed. Note the strong trend of the decrease in the SSP deviation from the ground truth as κ_3 approaches its global minimum in Fig. 13(b). For the optimal solution $c_3(z)$, rms deviation from $C_1(z)$ is about 1/3 of the deviation at $\kappa_3 = 2.365$ m/s.

Sensitivity of the cost function κ_3 [Eq. (6)] (and, hence, of the deviation of the inverse problem solution from the ground truth) to the unknown EOF amplitudes α_j is illustrated in Fig. 13(c). The amplitudes α_1 and α_2 of the first two EOFs, which together account for 83% of SSP variability [Fig. 11(b)], as well as the amplitude α_4 of the fourth EOF, rapidly and steadily approach their optimal values as κ_3 decreases in the course of the inversion process [Fig. 13(c)]. This contrasts with the wider and more symmetrical distribution of points in similar plots [Fig. 12(a)] in the synthetic data inversion, where no physical constraints were imposed. With the constraints, changes in α_1 and α_2 from one generation to the next prove to be highly correlated, which ensures a strong positive correlation between κ_3 and the SSP deviation from $C_1(z)$ and makes the inversion more robust.

The depth dependence of the uncertainty in the retrieved sound speed is shown in Fig. 13(d) by horizontal error bars, which are calculated with a 1 m vertical resolution. The error bars show $\pm\,\sigma$ standard deviation of the sound speed at each depth. The standard deviation is calculated for the same set of $\boldsymbol{\alpha}$ values as in Fig. 13(b). At almost all depths, the error bars are smaller than the difference between the initial reference SSP $C_2(z)$ and the ground truth $C_1(z)$ [see Fig. 13(d)]. Thus, the errors in passive measurements of the mode dispersion curves are sufficiently small to allow a meaningful SSP inversion. For most, but not all depths, the ground-truth SSP $C_1(z)$ lies within one standard deviation (i.e., the measurement uncertainty) of the optimum inversion result $c_3(z)$ [Fig. 13(d)].

The retrieved SSP $c_3(z)$ correctly reproduces the general shape of the ground-truth SSP $C_1(z)$ [Fig. 13(d)]. Both SSPs have a mixed layer and sharp thermocline and reach their respective minima at the same depth $z = 34$ m, where $C_1 - c_3 = 1.6$ m/s. The sound speed gradient in and position of the thermocline are particularly well reproduced by the inversion [Fig. 13(d)]. Comparison of Figs. 12(c) and 13(d) shows that inversions of synthetic (exact) and measured dispersion curves result in similar deviations from $C_1(z)$ in the mixed layer. Therefore, we attribute these deviations in the passively measured SSP to the weak sensitivity of the dispersion curves (Sec. IV B 1) of the low-order normal modes 1–3 and within the frequency range of 10–110 Hz of available data to the exact value of the sound speed in the mixed layer. In contrast, the excellent reconstruction of the thermocline reflects sensitivity of the dispersion curves to this part of the SSP.

The depth-averaged RMS deviation of $c_3(z)$ from $C_1(z)$ equals 1.48 m/s, when averaged over the entire water column. This RMSE is comparable to the 1.36 m/s RMSE in matching synthetic dispersion curves using the same SSP parameterization (Sec. IV B 1). When $C_1(z)$ and $c_3(z)$ are compared only at depths of $15\text{ m} < z < 82$ m below the mixed layer, the rms deviation decreases slightly to 1.41 m/s. It proves to be twice the rms deviation of $c_2(z)$ from $C_1(z)$ in the same depth range (Sec. IV B 1). We attribute this increase in the deviation of the inversion result $c_3(z)$ from the ground truth to the group speed measurement errors. Taken together, comparison of the RMSEs in two depth ranges suggests that limitations of the SSP parameterization and the errors of the mode dispersion curve measurements make comparable contributions to the overall errors of the passive acoustic SSP retrieval.

Taking advantage of noise records of opportunity, the inverse problem considered in this paper models the scheme of passive acoustic monitoring of the coastal ocean, where sound speed in water is measured in the beginning (or the end) of a long period of observations and is passively monitored from that point forward (correspondingly, recovered retrospectively) using NI. Retrieval of SSP and its sub-seasonal variations from EGFs (Sec. IV) has been made possible by application of the time-warping transform to separate normal modes and passively measure the frequency dependence of their group speeds. This technique (Tan *et al.*, 2019; Tan *et al.*, 2020), which is specific to shallow water, retrieves much more environmentally sensitive information from NCCFs than measuring positions of a few maxima (Evers *et al.*, 2017; Li *et al.*, 2019) or zero crossings (Godin *et al.*, 2010) of the time-domain EGF. Accurate passive measurements of the sound speed in water have been also assisted by availability of multiple receivers and, hence, multiple propagation paths in the horizontal plane, which allowed us to decrease the errors in measurements of the normal mode dispersion curves [Fig. 13(a)].

To our knowledge, the passive SSP inversion reported in this paper is the first documented example of successful passive acoustic tomography of the water column in shallow water, where only acoustic data is used as input for inversion. We show that NI-based passive acoustic measurement of a time-averaged SSP and its sub-seasonal variations are feasible even when internal gravity waves and internal tides cause strong, transient sound-speed variations during the noise averaging period. Compared to previous experimental work on passive ocean acoustic tomography (Godin *et al.*, 2010), which relied on direct rays in deep water, SSP is restored here under much more complicated propagation conditions and at ranges that are large compared to the water depth. We have retrieved depth-dependence of the sound speed from passive acoustic data in contrast to (Li *et al.*, 2019), where only spatially averaged sound speed was measured acoustically. By using the normal mode approach, we

have removed the limitations of the earlier work (Goncharov *et al.*, 2016), where application of ray tomography to EGFs was found to give less reliable SSP inversions with the low-frequency data provided by NI in shallow water.

VI. CONCLUSION

This paper has investigated passive acoustic characterization of coastal ocean dynamics. We have compared the environmental information that is contained in the NCCFs, which were obtained in two non-overlapping, 15-day observation periods by the same set of hydrophones on the continental shelf off New Jersey. The time-warping transform has been used to passively measure dispersion curves of normal modes and maximize the retrieval of oceanographically relevant information from noise cross-correlations. By comparing results of passive geoacoustic inversions, we have demonstrated that clearly distinct NCCFs contain consistent information about the seabed and lead to equivalent geoacoustic models.

Passively measured group speeds of acoustic normal modes have been inverted to retrieve the time-average of the SSP in water during one of the noise observation periods. Using the traditional contact temperature measurements as the ground truth, we have demonstrated that purely acoustic, passive sound-speed measurements are sufficiently accurate to quantitatively characterize the sub-seasonal variations of the average SSP between the two observation periods. The sub-seasonal SSP variations have been successfully measured under challenging conditions, where strong nonlinear internal waves repeatedly caused transient, rapid sound speed variations with magnitudes comparable to and even larger than the sub-seasonal variations.

The results of passive acoustic tomography of the water column, which are reported in this paper, complement the previously published results of passive geoacoustic inversions (Tan *et al.*, 2020) at the site and demonstrate the feasibility of NI-based passive acoustic monitoring of ocean dynamics on the continental shelf.

Further research is needed to improve the time resolution of the NI-based passive acoustic remote sensing of the ocean and to add a horizontal resolution of the sound speed field to the vertical and temporal resolution demonstrated in this paper. A promising way to decrease the noise averaging time, which is necessary for retrieval of EGFs with oceanographically relevant accuracy, is to employ machine learning techniques (Bianco *et al.*, 2019) to automatically identify and select short observation periods where the recorded noise field is sufficiently diffuse.

ACKNOWLEDGMENT

The authors are grateful to Y.-T. Lin and Arthur Newhall (Woods Hole Oceanographic Institution) for guidance on the SW06 data, and to Roberto Cristi (Naval Postgraduate School) for useful discussion of the EOF technique. This research has been supported by the Office of Naval Research, awards N00014-18-WX-01725 and N00014-19-WX00462, the National Science Foundation, award OCE1657430, and the Taiwan Ministry of Science and Technology, Grant No. 109-2611-M-012-002.

APPENDIX: GEOACOUSTIC INVERSION BASED ON THE DATA ACQUIRED IN THE FIRST OBSERVATION PERIOD

The previous work (Tan *et al.*, 2020) used the N-NCCF$_2$ in Fig. 4(b) and the corresponding average $C_2(z)$ of the measured SSPs in Fig. 2(b) to retrieve the geoacoustic properties of seabed. We refer to the results of that inversion as the geoacoustic model GM$_2$. Here, we apply the same approach to N-NCCF$_1$, which is obtained in the first observation period, and compare the resulting geoacoustic model GM$_1$ with the model GM$_2$. In contrast to the main text, the average SSP $C_1(z)$ in the water column will be assumed known in the course of the geoacoustic inversion.

The group speeds $g_{i,m}(f) = r_i/\tau_{i,m}(f)$ of modes $m = 1$–3 retrieved from the N-NCCF$_1$, described in Sec. III A, are averaged as $\bar{g}_m(f)$ and used as input data for geoacoustic inversion. Here, r_i and $\tau_{i,m}$ are the horizontal distance and measured modal travel time, respectively, between the SHRU and the ith HLA hydrophone with $i = 1, 2,\ldots,32$ [Fig. 1(b)]. The inverse problem is assuming range-independent [Fig. 14(a)] where the impact of modal travel times from horizontal inhomogeneity in a simulation is small even in this dynamic environment, and discussed previously in Sec. III D.

The unknown geoacoustic parameters are put into a vector GM$_1$ found by minimizing the cost function K(GM$_1$), which is Eq. (3) of Tan *et al.* (2020) between the measured $\bar{g}_m(f)$ extracted from NCCF$_1$ through the time-warping transform (Sec. III A) and modeled group speeds $\hat{g}_m$ of normal modes. Here, $M = 3$ is the number of normal modes identified in Sec. III A, and N_m is the number of frequency bins to be compared between the measured $\bar{g}_m(f)$ and the modeled dispersion curves $\hat{g}_m$ of mode m. The $C_1(z)$ is a measured and known parameter [Fig. 2(b)] during the inversion process. Non-overlapping bins of ~0.2 Hz width are used in the 10–110, 25–110, and 40–110 Hz frequency bands for modes 1, 2, and 3, respectively. The modeled group speeds $\hat{g}_m(f_n, \text{GM}_1)$ are calculated using $C_1(z)$ by the normal mode code KRAKEN (Porter, 1992) for various values of the vector GM$_1$ = [D, H, c_s, ρ_s, c_b, ρ_b] to be inverted in the unknown range-independent environment [Fig. 14(a)]. The dispersion curves $\bar{g}_m(f)$ retrieved from N-NCCF$_1$ and N-NCCF$_2$ are different because the time-dependent average SSPs $C_1(z)$ and $C_2(z)$ are different only (Fig. 7); the inverted geoacoustic parameters GM$_1$ and GM$_2$ shall physically remain unchanged. Table III shows their discrepancies are within error bounds.

The array configuration of the HLA is not a perfectly taut straight line but is tilted during the experiment period (Newhall *et al.*, 2007; Duda *et al.*, 2012), and the horizontal distance correction Δr re-calibrates the average $\bar{g}_m(f)$ of the

https://doi.org/10.1121/10.0006664

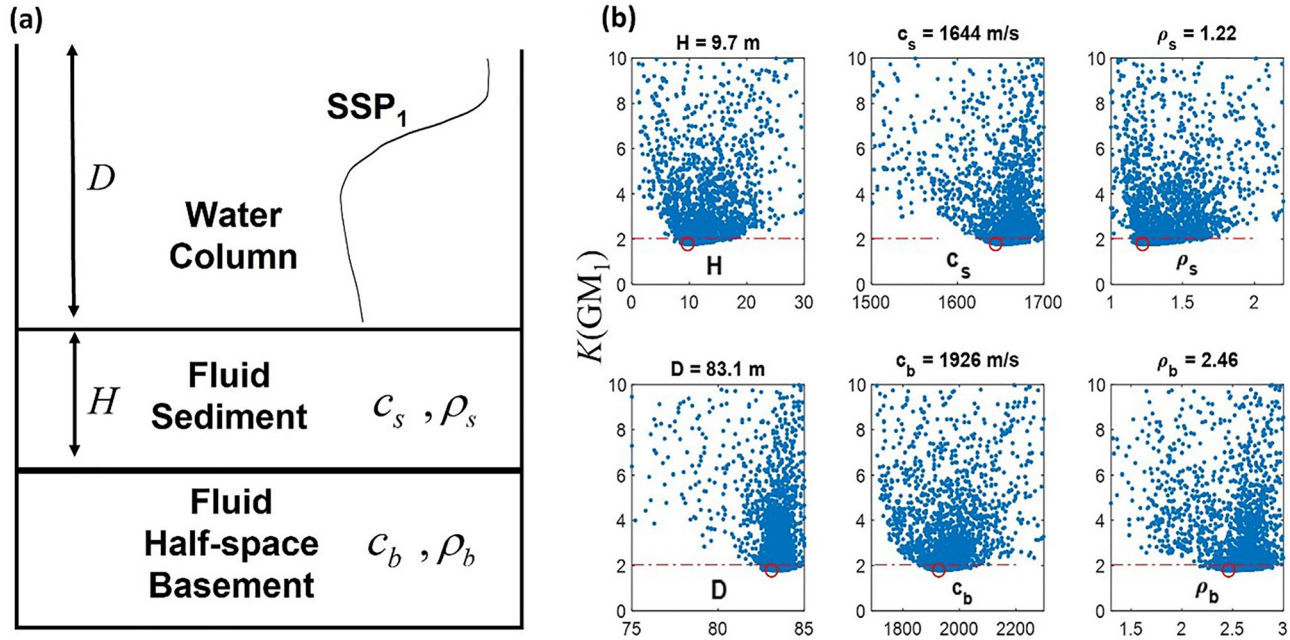

FIG. 14. (Color online) Geoacoustic inversion using N-NCCF$_1$. (a) Range-independent environmental model implied in the inverse problem. The six unknown parameters to be determined are the water depth D, sediment layer thickness H, sound speeds c_s, c_b in the sediment and basement, and the ratios ρ_s, ρ_b of densities in the sediment and basement to that in seawater. SSP $C_1(z)$ in water is assumed to be known. (b) Sensitivity of the data-model mismatch to individual parameters of the environmental model. In each panel, the cost function $K(\mathrm{GM}_1)$, is plotted as a function of a single search parameter for the values of the other six parameters that were encountered during the optimization process. The circle indicates the position of the cost function minimum and the inferred value of each parameter, which is shown on top of each sub-panel. The dashed line corresponds to the error bounds in Table III. Values of $K(\mathrm{GM}_1)$ up to 10 m/s are shown.

measured modal group speeds, which are applied to refine the precision of the retrieved group speeds $g_{i,m}(f) = (r_i + \Delta r)/\tau_{i,m}(f)$. The frequency dependence of the path-averaged group speeds $\bar{g}_m(f)$ is an average over $g_{i,m}(f)$, and this average significantly reduces random errors of measurement. In the previous study (Tan *et al.*, 2020), the differences between travel times $\tau_{i,m}(f)$ over actual, range-dependent bathymetry [Fig. 1(b)] on a path and in the range-independent waveguide with the path-averaged water depth [Fig. 14(a)] was shown to be small compared with the measurement errors on a single path. The previous inverted effective horizontal distance correction $\Delta r = 5.6$ m (Tan *et al.*, 2020) falls within the uncertainty of the GPS measurement for NCCF$_2$, and it is slightly adjusted to $\Delta r = 8.9$ m in the inverse problem of NCCF$_1$. This Δr adjustment is based on the best modal separation described in Sec. III A with an empirical observed $\tau_{r,i}$ and with the conclusion $g_{m=1}(f_{\max}) \cong C_{1\min} = 1487.9$ m/s. This minimum value of SSP, $C_{1\min}$ is used to obtain the effective horizontal distance correction Δr by best-fitting each measured $\tau_{r,i} = (r_i + \Delta r)/C_{1\min}$ for each SHRU-ith HLA hydrophone path. This Δr is off by 3.3 m (Table III) between NCCF$_1$ and NCCF$_2$ acoustic observation, which could be due to the temporal distance uncertainty measured between the SHRU and the HLA, as well as the HLA shape anomalies seen in Fig. 12 of Duda *et al.* (2012), primarily due to internal wave activity during the two observation periods.

A MATLAB-based genetic algorithm was used to find the global minimum of the cost function. The global minimum was found as $K(\mathrm{GM}_1) \approx 1.7881$ m/s. Search bounds and results are summarized in Table III with the previous study (Tan *et al.*, 2020). The choice of the search bounds for the geoacoustic parameters was informed by the results of the previous geoacoustic studies (Huang *et al.*, 2008; Jiang and Chapman, 2008; Jiang *et al.*, 2010; Bonnel and Chapman, 2011) and the meta study of Bonnel *et al.* (2020a) at the SW06 site. Figure 14(b) illustrates the sensitivity of the cost function $K(\mathrm{GM}_1)$ to variations of individual search parameters around the optimal environmental model. We compare the increase in the cost function $K(\mathrm{GM}_1)$ from its minimal value to the measurement errors to estimate the uncertainty of the inversion results. The rms measurement error of path-averaged modal group speeds is plotted as a dashed-line in each sub-panel of Fig. 14(b). The inversion error bounds are summarized in Table III.

As a function of water depth D, the mismatch is minimal at $D = 83.1$ m. This value is close to the water depth at the SHRU location and close to the average water depth, along the propagation paths shown in Fig. 1(b) within tidal tolerance. The other retrieved geoacoustic values of seabed, [H, c_s, ρ_s, c_b, ρ_b] of GM$_1$ in Table III, also fall within the error bounds of GM$_2$, and *vice versa* for the retrieved seabed properties of GM$_2$. The results in Table III demonstrate that, despite significant variations in the water column properties and in the NCCFs, which are obtained in non-overlapping observation periods, the geoacoustic information contained in distinct NCCFs remains consistent and that NI-based geoacoustic inversion is robust. Furthermore, consistency of the geoacoustic models GM$_1$ and GM$_2$ justifies the use of the

previously established seabed model GM_2 in conjunction with $NCCF_1$ for the purposes of the passive acoustic characterization of the water column in the first observation period, which is considered in the main text.

Ballard, M. S., Frisk, G. V., and Becker, K. M. (**2014**). "Estimates of the temporal and spatial variability of ocean sound speed on the New Jersey shelf," J. Acoust. Soc. Am. **135**, 3316–3326.

Baraniuk, R. G., and Jones, D. L. (**1995**). "Unitary equivalence: A new twist on signal processing," IEEE Trans. Signal Process. **43**, 2269–2282.

Bianco, M. J., Gerstoft, P., Traer, J., Ozanich, E., Roch, M. A., Gannot, S., and Deledalle, C.-A. (**2019**). "Machine learning in acoustics: Theory and applications," J. Acoust. Soc. Am. **146**, 3590–3628.

Bonnel, J., Caporale, S., and Thode, A. (**2017**). "Waveguide mode amplitude estimation using warping and phase compensation," J. Acoust. Soc. Am. **141**, 2243–2255.

Bonnel, J., and Chapman, N. R. (**2011**). "Geoacoustic inversion in a dispersive waveguide using warping operators," J. Acoust. Soc. Am. **130**, EL101–EL107.

Bonnel, J., Dosso, S. E., Eleftherakis, D., and Chapman, N. R. (**2019**). "Trans-dimensional inversion of modal dispersion data on the New England mud patch," IEEE J. Oceanic Eng. **45**, 116–130.

Bonnel, J., Pecknold, S. P., Hines, P. C., and Chapman, N. R. (**2020a**). "An experimental benchmark for geoacoustic inversion methods," IEEE J. Oceanic Eng. **46**, 261–282.

Bonnel, J., Thode, A., Wright, D., and Chapman, R. (**2020b**). "Nonlinear time-warping made simple: A step-by-step tutorial on underwater acoustic modal separation with a single hydrophone," J. Acoust. Soc. Am. **147**, 1897–1926.

Brekhovskikh, L. M., and Godin, O. A. (**1999**). *Acoustics of Layered Media. 2. Point Sources and Bounded Beams* (Springer, New York), pp. 174–177.

Brooks, L. A., and Gerstoft, P. (**2009**). "Green's function approximation from cross-correlations of 20–100 Hz noise during a tropical storm," J. Acoust. Soc. Am. **125**, 723–734.

Brown, M. G. (**2020**). "Time-warping in underwater acoustic waveguides," J. Acoust. Soc. Am. **147**, 898–910.

Brown, M. G., Godin, O. A., Williams, N. J., Zabotin, N. A., Zabotina, L., and Banker, G. J. (**2014**). "Acoustic Green's function extraction from ambient noise in a coastal ocean environment," Geophys. Res. Lett. **41**, 5555–5562, https://doi.org/10.1002/2014GL060926.

Brown, M. G., Godin, O., Zang, X., Ball, J., Zabotin, N., Zabotina, L., and Williams, N. (**2016**). "Ocean acoustic remote sensing using ambient noise: Results from the Florida Straits," Geophys. J. Int. **206**, 574–589.

Dong, H., Badiey, M., and Chapman, N. R. (**2016**). "Geoacoustic inversion of airgun data under influence of internal waves," IEEE J. Oceanic Eng. **42**, 632–638.

Duan, R., Ross Chapman, N., Yang, K., and Ma, Y. (**2016**). "Sequential inversion of modal data for sound attenuation in sediment at the New Jersey Shelf," J. Acoust. Soc. Am. **139**, 70–84.

Duda, T. F., Collis, J. M., Lin, Y.-T., Newhall, A. E., Lynch, J. F., and DeFerrari, H. A. (**2012**). "Horizontal coherence of low-frequency fixed-path sound in a continental shelf region with internal-wave activity," J. Acoust. Soc. Am. **131**, 1782–1797.

Evers, L. G., Wapenaar, K., Heaney, K. D., and Snellen, M. (**2017**). "Deep ocean sound speed characteristics passively derived from the ambient acoustic noise field," Geophys. J. Int. **210**, 27–33.

Fried, S. E., Kuperman, W., Sabra, K. G., and Roux, P. (**2008**). "Extracting the local Green's function on a horizontal array from ambient ocean noise," J. Acoust. Soc. Am. **124**, EL183–EL188.

Fulop, S. A., and Fitz, K. (**2006**). "Algorithms for computing the time-corrected instantaneous frequency (reassigned) spectrogram, with applications," J. Acoust. Soc. Am. **119**, 360–371.

Gerstoft, P., Hodgkiss, W. S., Siderius, M., Huang, C.-F., and Harrison, C. H. (**2008**). "Passive fathometer processing," J. Acoust. Soc. Am. **123**, 1297–1305.

Godin, O. A. (**2006**). "Recovering the acoustic Green's function from ambient noise cross correlation in an inhomogeneous moving medium," Phys. Rev. Lett. **97**, 054301.

Godin, O. A. (**2009**). "Accuracy of the deterministic travel time retrieval from cross-correlations of non-diffuse ambient noise," J. Acoust. Soc. Am. **126**, EL183–EL189.

Godin, O. A. (**2010**). "Cross-correlation function of acoustic fields generated by random high-frequency sources," J. Acoust. Soc. Am. **128**, 600–610.

Godin, O. A. (**2018**). "Acoustic noise interferometry in a time-dependent coastal ocean," J. Acoust. Soc. Am. **143**, 595–604.

Godin, O. A., Brown, M. G., Zabotin, N. A., Zabotina, L. Y., and Williams, N. J. (**2014**). "Passive acoustic measurement of flow velocity in the Straits of Florida," Geosci. Lett. **1**, 16.

Godin, O. A., Katsnelson, B., Qin, J., Brown, M. G., Zabotin, N., and Zang, X. (**2017**). "Application of time reversal to passive acoustic remote sensing of the ocean," Acoust. Phys. **63**, 309–320.

Godin, O. A., Katsnelson, B., and Tan, T. W. (**2019**). "Normal mode dispersion and time warping in the coastal ocean," J. Acoust. Soc. Am. **146**, EL205–EL211.

Godin, O. A., Zabotin, N. A., and Goncharov, V. V. (**2010**). "Ocean tomography with acoustic daylight," Geophys. Res. Lett. **37**, L13605, https://doi.org/10.1029/2010GL043623.

Godin, O. A., Zavorotny, V. U., Voronovich, A. G., and Goncharov, V. V. (**2006**). "Refraction of sound in a horizontally inhomogeneous, time-dependent ocean," IEEE J. Oceanic Eng. **31**, 384–401.

Goncharov, V., Shurup, A., Godin, O., Zabotin, N., Vedenev, A., Sergeev, S., Brown, M. G., and Shatravin, A. (**2016**). "Tomographic inversion of measured cross-correlation functions of ocean noise in shallow water using ray theory," Acoust. Phys. **62**, 436–446.

Guarino, A. L., Smith, K. B., and Godin, O. A. (**2021**). "Bottom attenuation coefficient inversion based on the modal phase difference between pressure and vertical velocity from a single vector sensor," J. Theor. Comput. Acoust. **25**, 2150008.

Harrison, C. H., and Siderius, M. (**2008**). "Bottom profiling by correlating beam-steered noise sequences," J. Acoust. Soc. Am. **123**, 1282–1296.

Huang, C.-F., Gerstoft, P., and Hodgkiss, W. S. (**2008**). "Effect of ocean sound speed uncertainty on matched-field geoacoustic inversion," J. Acoust. Soc. Am. **123**, EL162–EL168.

Jiang, Y.-M., and Chapman, N. R. (**2008**). "Bayesian geoacoustic inversion in a dynamic shallow water environment," J. Acoust. Soc. Am. **123**, EL155–EL161.

Jiang, Y.-M., and Chapman, N. R. (**2009**). "The impact of ocean sound speed variability on the uncertainty of geoacoustic parameter estimates," J. Acoust. Soc. Am. **125**, 2881–2895.

Jiang, Y.-M., Chapman, N. R., and Gerstoft, P. (**2010**). "Estimation of geoacoustic properties of marine sediment using a hybrid differential evolution inversion method," IEEE J. Oceanic Eng. **35**, 59–69.

Katsnelson, B. G., Godin, O. A., and Zhang, Q. (**2021**). "Observations of acoustic noise bursts accompanying nonlinear internal gravity waves on the continental shelf off New Jersey," J. Acoust. Soc. Am. **149**, 1609–1622.

Le Touzé, G. É., Nicolas, B., Mars, J. I., and Lacoume, J.-L. (**2009**). "Matched representations and filters for guided waves," IEEE Trans. Signal Process. **57**, 1783–1795.

Li, F., Wang, K., Yang, X., Zhang, B., and Zhang, Y. (**2021**). "Passive ocean acoustic thermometry with machine learning," Appl. Acoust. **181**, 108167.

Li, F., Yang, X., Zhang, Y., Luo, W., and Gan, W. (**2019**). "Passive ocean acoustic tomography in shallow water," J. Acoust. Soc. Am. **145**, 2823–2830.

Newhall, A. E., Duda, T. F., von der Heydt, K., Irish, J. D., Kemp, J. N., Lerner, S. A., Liberatore, S. P., Lin, Y.-T., Lynch, J. F., and Maffei, A. R. (**2007**). "Acoustic and oceanographic observations and configuration information for the WHOI moorings from the SW06 experiment," Woods Hole Oceanographic Institution, Falmouth, MA.

Nichols, B., Martin, J., Verlinden, C., and Sabra, K. G. (**2019**). "Enhancing ambient noise correlation processing using vector sensors," J. Acoust. Soc. Am. **145**, 3567–3577.

Niu, H., Zhang, R., and Li, Z. (**2014**). "Theoretical analysis of warping operators for non-ideal shallow water waveguides," J. Acoust. Soc. Am. **136**, 53–65.

Nowakowski, T., Daudet, L., and de Rosny, J. (**2015**). "Localization of acoustic sensors from passive Green's function estimation," J. Acoust. Soc. Am. **138**, 3010–3018.

Porter, M. B. (**1992**). *The KRAKEN Normal Mode Program* (Naval Research Lab, Washington DC).
Qin, J.-X., Katsnelson, B., Godin, O., and Li, Z.-L. (**2017**). "Geoacoustic inversion using time reversal of ocean noise," Chin. Phys. Lett. **34**, 094301.
Roux, P., Kuperman, W., and Group, N. (**2004**). "Extracting coherent wave fronts from acoustic ambient noise in the ocean," J. Acoust. Soc. Am. **116**, 1995–2003.
Sabra, K. G., Roux, P., and Kuperman, W. (**2005a**). "Arrival-time structure of the time-averaged ambient noise cross-correlation function in an oceanic waveguide," J. Acoustical Soc. America **117**, 164–174.
Sabra, K. G., Roux, P., and Kuperman, W. (**2005b**). "Emergence rate of the time-domain Green's function from the ambient noise cross-correlation function," J. Acoust. Soc. Am. **118**, 3524–3531.
Sabra, K. G., Roux, P., Thode, A. M., D'Spain, G. L., Hodgkiss, W., and Kuperman, W. (**2005c**). "Using ocean ambient noise for array self-localization and self-synchronization," IEEE J. Oceanic Eng. **30**, 338–347.
Sergeev, S., Shurup, A., Godin, O., Vedenev, A., Goncharov, V., Mukhanov, P. Y., Zabotin, N., and Brown, M. G. (**2017**). "Separation of acoustic modes in the Florida Straits using noise interferometry," Acoust. Phys. **63**, 76–85.
Siderius, M., Harrison, C. H., and Porter, M. B. (**2006**). "A passive fathometer technique for imaging seabed layering using ambient noise," J. Acoust. Soc. Am. **120**, 1315–1323.
Siderius, M., Song, H., Gerstoft, P., Hodgkiss, W. S., Hursky, P., and Harrison, C. (**2010**). "Adaptive passive fathometer processing," J. Acoust. Soc. Am. **127**, 2193–2200.
Skarsoulis, E., and Cornuelle, B. (**2019**). "Cross-correlation of shipping noise: Refraction and receiver-motion effects," J. Acoust. Soc. Am. **145**, 3003–3010.
Skarsoulis, E., and Cornuelle, B. (**2020**). "Cross-correlation sensitivity kernels with respect to noise source distribution," J. Acoust. Soc. Am. **147**, 1–9.
Snapper, E., and Troyer, R. J. (**2014**). *Metric Affine Geometry* (Elsevier, Amsterdam, the Netherlands).
Tan, T. W., Godin, O. A., Brown, M. G., and Zabotin, N. A. (**2019**). "Characterizing the seabed in the Straits of Florida by using acoustic noise interferometry and time warping," J. Acoust. Soc. Am. **146**, 2321–2334.
Tan, T. W., Godin, O. A., Katsnelson, B., and Yarina, M. (**2020**). "Passive geoacoustic inversion in the Mid-Atlantic Bight in the presence of strong water column variability," J. Acoust. Soc. Am. **147**, EL453–EL459.
Tang, D., Moum, J. N., Lynch, J. F., Abbot, P., Chapman, R., Dahl, P. H., Duda, T. F., Gawarkiewicz, G., Glenn, S., and Goff, J. A. (**2007**). "Shallow Water '06: A joint acoustic propagation/nonlinear internal wave physics experiment," Oceanography **20**, 156–167.
Wapenaar, K., and Thorbecke, J. (2013). "On the retrieval of the directional scattering matrix from directional noise," SIAM J. **6**, 322–340.
Weaver, R., Froment, B., and Campillo, M. (**2009**). "On the correlation of non-isotropically distributed ballistic scalar diffuse waves," J. Acoust. Soc. Am. **126**, 1817–1826.
Woolfe, K. F., Lani, S., Sabra, K. G., and Kuperman, W. A. (**2015**). "Monitoring deep-ocean temperatures using acoustic ambient noise," Geophys. Res. Lett. **42**, 2878–2884, https://doi.org/10.1002/2015GL063438.
Yang, X., Li, F., Zhang, B., and Luo, W. (**2020**). "Seasonally-invariant head wave speed extracted from ocean noise cross-correlation," J. Acoust. Soc. Am. **147**, EL241–EL245.
Yardim, C., Gerstoft, P., Hodgkiss, W. S., and Traer, J. (**2014**). "Compressive geoacoustic inversion using ambient noise," J. Acoust. Soc. Am. **135**, 1245–1255.
Zang, X., Brown, M. G., and Godin, O. A. (**2015**). "Waveform modeling and inversion of ambient noise cross-correlation functions in a coastal ocean environment," J. Acoust. Soc. Am. **138**, 1325–1333.
Zeng, J., Chapman, N. R., and Bonnel, J. (**2013**). "Inversion of seabed attenuation using time-warping of close range data," J. Acoust. Soc. Am. **134**, EL394–EL399.
Zhou, J., Piao, S., Qu, K., Iqbal, K., Dong, Y., Zhang, S., Zhang, H., Wang, X., and Liu, Y. (**2017**). "Extracting the time domain Green's function from ocean ambient noise using acoustic vector sensors," J. Acoust. Soc. Am. **142**, EL507–EL511.